Simon Erker, BSc

Correlated Electronic Structure of Manganese Pnictides

Master Thesis

For obtaining the academic degree
Diplom-Ingenieur

Master Programme of
Technical Physics

Graz University of Technology

Supervisor:
Prof. Dr. Enrico Arrigoni
Co-Supervisor:
Dr. Markus Aichhorn
Institute of Theoretical and Computational Physics

Graz, February 2014

Statutory Declaration

I, Simon Erker, declare that I have authored this thesis independently, that I have not used other than the declared sources / resources, and that I have explicitly marked all material which has been quoted either literally or by content from the used sources.

Signed: _____

Date: _____

Abstract

Correlated Electronic Structure of Manganese Pnictides

by Simon Erker

Density functional theory (DFT) within the local density approximation (LDA) describes well the electronic structure of many weakly correlated materials but completely fails for materials that are *strongly correlated*. Typically these strongly correlated materials have partially filled *d*- or *f*-shells where the Coulomb interaction is comparable to the bandwidth. One of the most successful techniques for modeling strongly correlated electron systems is the dynamical mean-field theory (DMFT). Combining DMFT with the *ab-initio* LDA-scheme is an efficient method to go beyond DFT and include local correlations.

In this thesis the basic LDA+DMFT scheme is explained and the method is used to calculate the electronic structure of the manganese based pnictide materials $BaMn_2As_2$ and LaOMnAs. A continuous-time quantum Monte Carlo (CT-QMC) algorithm in the hybridization expansion at room temperature ($\beta = 40$ eV^{-1}) considering only density-density interactions is used to obtain the momentum resolved and momentum integrated spectral functions.

For $BaMn_2As_2$ we used the *dp*-model corresponding to the experimental crystal structure and investigated the influence of the selected energy window, the double counting correction and of the interaction parameters U and J.

For LaOMnAs we showed the difference of the *dpp*-model and the *d*-model for the description of the electronic structure.

to my ever supportive parents . . .

Contents

Introduction

The physics of materials with electrons that are strongly correlated is a very interesting and emerging topic in today's theoretical and experimental condensed matter physics. Strongly correlated materials often show unusual electronic and magnetic properties such as superconductivity, metal-insulator transitions, half-metallicity or heavy-fermion behavior. These rich phenomena put correlated materials in the focus of experimental research and give a motivation for a better theoretical understanding of these materials. Transition metal compounds with their partially filled d-shells are a typical candidate for strong electronic correlations. An essential feature that combines all these materials is that the behavior of their electrons cannot be described effectively by conventional band structure methods like density functional theory (DFT) in the local density approximation (LDA). One must go beyond DFT-LDA and include electronic correlation to achieve accurate results for the electronic structure. Many-body methods are capable to explicitly treat electronic correlations. A successful many-body method in this context is the dynamical mean-field theory (DMFT) that maps a lattice model onto a self-consistent determined impurity model. DMFT fully accounts for local correlations and becomes exact in the limit of infinite dimensions. However, many-body methods only work for simplified effective models and depend on unknown model parameters. Therefore they cannot provide an *ab-initio* description of real materials. An approach that elude this problems and was developed in the last years is the LDA+DMFT method. It combines the advantages of DFT-LDA, that provides a realistic ab-initio description for many weakly correlated materials, with the correct treatment of local correlations within DMFT. The main topic of this thesis is to investigate the electronic structure of strongly correlated transition metal compounds with this LDA+DMFT approach. In particular, the strongly correlated manganese-based pnictide materials $BaMn_2As_2$ and LaOMnAs are studied. The impurity problem within the self-consistent DMFT equations is solved with a continuous-time quantum Monte Carlo algorithm in the hybridization expansion.

Outline of this thesis

This thesis is split into two parts. Part I is a review of the applied methods and in part II we show some applications on manganese-based pnictides.
In chapter 1, the theoretical background of density functional theory is reviewed and the limitations of the local density approximation for strongly correlated materials are discussed.
In chapter 2, a summary of the dynamical mean field theory based on the Hubbard model is given. Furthermore, the basics of continuous-time quantum Monte Carlo is explained, which is used for solving the impurity problem. Finally the maximum entropy method for obtaining the spectral function on the real axis is discussed.
In chapter 3, a fully charge self-consistent implementation of the LDA+DMFT scheme is presented. It combines the conventional band structure package WIEN2K with the TRIQS library for interacting quantum systems.
In part II, chapters 4 and 5 discuss applications of DFT and LDA+DMFT to the manganese-based pnictide materials $BaMn_2As_2$ and LaOMnAs, respectively. Starting with the crystal and magnetic structure of those materials, the densities of states and band structures obtained by LDA are studied. Finally the spectral functions obtained with LDA+DMFT are presented.

Part I

Methods

Chapter 1

Conventional electronic structure calculations

1.1 Introduction

In condensed matter physics it is in principle easy to write down the starting point for all quantitative calculations of electronic properties:

$$\hat{H}\,|\Psi\rangle = E\,|\Psi\rangle \tag{1.1}$$

This eigenvalue problem describes the quantum nature of matter, where $\hat{H}$ is the Hamiltonian of the system. The full Hamiltonian of a condensed matter system is given, in atomic units, by

$$\hat{H} = -\frac{1}{2}\sum_i \nabla_i^2 - \sum_\alpha \frac{1}{2M_\alpha}\nabla_\alpha^2 - \sum_{\alpha,i}\frac{Z_\alpha}{|\mathbf{r}_i - \mathbf{R}_\alpha|} + \frac{1}{2}\sum_{i,i'}\frac{1}{|\mathbf{r}_i - \mathbf{r}_{i'}|} + \frac{1}{2}\sum_{\alpha,\alpha'}\frac{Z_\alpha Z_{\alpha'}}{|\mathbf{R}_\alpha - \mathbf{R}_{\alpha'}|}$$

where $\mathbf{r}_i$ and $\mathbf{R}_\alpha$ denote the position of electron i and atomic nuclei α with atomic number Z_α and nuclear mass M_α. The first two terms describe the kinetic energy of the electrons and the nuclei, respectively. The third terms, the lattice potential, describes the interaction of the electrons with the nuclei, the fourth term the electron-electron interaction and the last term the interaction between the nuclei.

Now the fundamental problem in condensed matter physics is solving the Schrödinger equation (1.1). However, the many-body nature of the problem makes finding the solution, except in the simplest cases, impossible in practice. Even after applying the so called

Born-Oppenheimer approximation, by decoupling the electronic degrees of freedom from the lattice part, finding a solution of the Hamiltonian is far from being possible. This is because of the Coulomb term which describes the interaction between the electrons. It correlates every electron with all others and leads to a complex many-body problem. To solve this many-body problem one can either make substantial approximations to the Hamiltonian or replace it with a significantly simplified model Hamiltonian. Both approaches are used for the investigation of electronic properties in solids, in the density functional theory (DFT) and in many-body theory, respectively.

1.2 Density Functional Theory

The main motivation for using Density Functional Theory is that the calculations can be done from *first principles* which means the only input parameters are atomic numbers and the positions of the atoms in the crystal. The basis of DFT are the Hohenberg-Kohn theorems [1]:

> *The ground state electron density of a many electron system in the presence of an external potential uniquely determines the external potential.*

> *The functional for the ground state energy is minimized by the ground state electron density.*

The first Hohenberg-Kohn theorem states that the density may be used as the basic variable uniquely characterizing the system. From the second theorem one can derive that all ground state properties of any interacting electron gas can be described by minimizing the total energy as a functional of electron density $\rho(\mathbf{r})$. So the Hohenberg-Kohn theorems provide us with the basics for calculating properties of an interacting electron system. This can be realized in the framework of the Kohn-Sham approach [2]. The key idea of the Kohn-Sham approach is to replace the interacting many-body system with a simpler auxiliary system of non-interacting quasiparticles that has the same ground-state density as the true interacting system.

According to the Hohenberg-Kohn theorem and assuming the existence of such an auxiliary system, the energy functional of an interacting system can be written as a sum of

contributions:

$$E[\rho] = E_{kin}[\rho] + E_{ion}[\rho] + E_{hartree}[\rho] + E_{xc}[\rho] \tag{1.2}$$

with

$$E_{ion}[\rho] = \int d\mathbf{r}\rho(\mathbf{r})v^{ext}(\mathbf{r}) \tag{1.3}$$

$$E_{hartree}[\rho] = \int d\mathbf{r}\rho(\mathbf{r})v^{hartree}(\mathbf{r}) = \int d\mathbf{r}d\mathbf{r}'\frac{\rho(\mathbf{r})\rho(\mathbf{r}')}{|\mathbf{r}-\mathbf{r}'|} \tag{1.4}$$

where $E_{kin}[\rho]$ is the kinetic energy and $E_{ion}[\rho]$ is the energy of the electrons in the external potential v^{ext} of the ions. $E_{hartree}[\rho]$ describes the classical Coulomb interaction energy (Hartree energy) corresponding to the charge distribution ρ, i.e. it is the static mean-field contribution where an electron feels the potential $v^{hartree}$ induced by all other electrons. Finally $E_{xc}[\rho]$ is the so called exchange-correlation energy in which all difficulties of the quantum many-body problem, comprising exchange and correlation effects, are transferred.

From this we can introduce the Kohn-Sham potential. It is the single-particle potential that will lead to the same density $\rho(\mathbf{r})$ as the original interacting problem.

$$v^{KS}[\rho(\mathbf{r})] = v^{ext}(\mathbf{r}) + v^{hartree}(\mathbf{r}) + v^{xc}[\rho](\mathbf{r}) \tag{1.5}$$

where the exchange-correlation potential v^{xc} is defined as the functional derivative of the exchange-correlation energy $E_{xc}[\rho]$:

$$v^{xc}[\rho](\mathbf{r}) = \frac{\delta E_{xc}[\rho]}{\delta\rho(\mathbf{r})} \tag{1.6}$$

To be able to express the kinetic energy E_{kin}, which cannot explicitly expressed in terms of the electron density, we perform the minimization of the energy functional $E[\rho]$ with respect to a set of one-particle wave functions $\psi_{\mathbf{k}\nu}(\mathbf{r})$ instead of the density $\rho(\mathbf{r})$. These normalized set of wave functions fulfill

$$\rho(\mathbf{r}) = \sum_{\epsilon_{\mathbf{k}\nu}\leq\epsilon_F} |\psi_{\mathbf{k}\nu}(\mathbf{r})|^2. \tag{1.7}$$

The minimization finally leads to the following independent single-particle Schrödinger-like equations known as Kohn-Sham equations:

$$\left[-\frac{\hbar^2}{2m}\nabla^2 + v^{KS}[\rho]\right]\psi_{\mathbf{k}\nu}(\mathbf{r}) = \epsilon_{\mathbf{k}\nu}\psi_{\mathbf{k}\nu}(\mathbf{r}) \tag{1.8}$$

where $\psi_{\mathbf{k}\nu}(\mathbf{r})$ are the Kohn-Sham eigenfunctions of the one-particle system and $\epsilon_{\mathbf{k}\nu}(\mathbf{r})$ are the Kohn-Sham eigenstates. Hence, the complicated many-body problem is simplified to a set of non-interacting one-particle problems with a not explicitly known potential v^{xc}. It is important to note that up to this point no approximations were made and if v^{xc} or E_{xc} was known explicitly this mapping would be exact. However, in order to solve the Kohn-Sham equations (1.8) it is is necessary to find a suitable approximation for the exchange-correlations functional $E_{xc}[\rho]$. The most popular approximations in condensed matter physics are the local density approximation (LDA) and the generalized gradient approximation (GGA), which are briefly described in the next chapter.
With an approximation for $E_{xc}[\rho]$, the set of Kohn-Sham equations (1.8) has to be solved self-consistently. This is because the Kohn-Sham potential (1.5) is a functional of the density. The full self-consistent procedure is sketched in Fig. 1.1.

At this point it is important to note that the Kohn-Sham eigenfunctions $\psi_{\mathbf{k}\nu}$ and Kohn-Sham eigenvalues $\epsilon_{\mathbf{k}\nu}$ are quantities of the non-interacting auxiliary system which only has the same ground-state density as the original interacting system. Therefore they should not have any physical meaning. Nevertheless the Kohn-Sham eigenvalues $\epsilon_{\mathbf{k}\nu}$ often give surprisingly good results to describe the real excitation spectrum of the system and can therefore in fact be used to describe the real system, e.g. for calculating the band-structure.

1.3 Exchange-Correlation Functionals

Local Density Approximation

One of the most popular approximations to the exchange-correlation functional is the local density approximation (LDA) [2]:

$$E_{xc}^{LDA}[\rho] = \int d\mathbf{r}\rho(\mathbf{r})\epsilon_{xc}^{LDA}(\rho(\mathbf{r})) \tag{1.9}$$

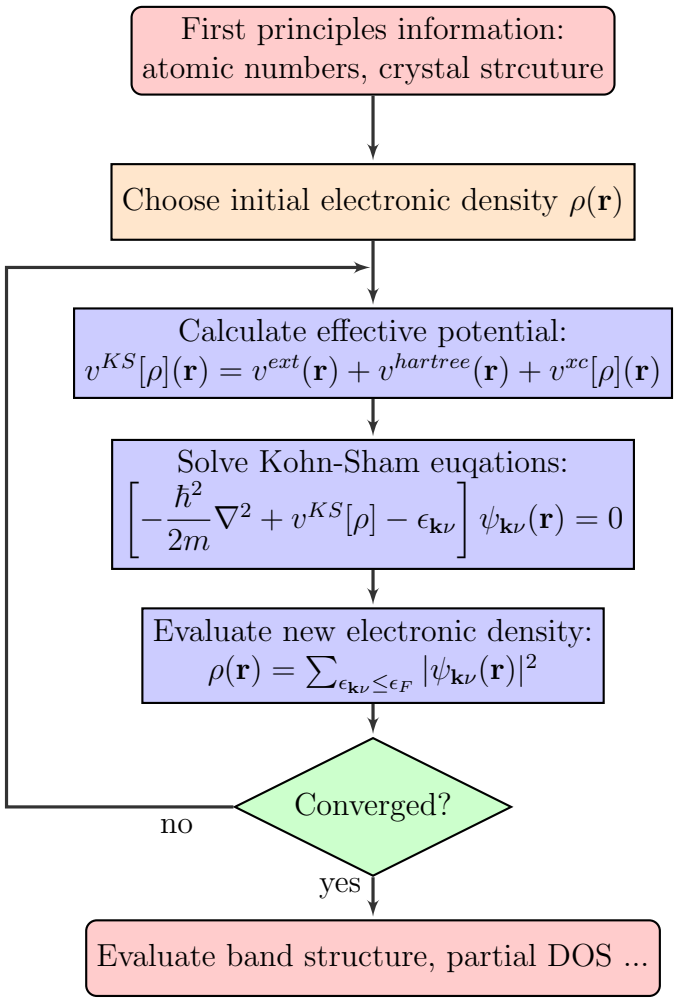

FIGURE 1.1: Flow chart of the DFT charge self-consistent scheme.

where $\epsilon_{xc}^{LDA}(\rho)$ is the exchange-correlation energy density of the homogeneous electron gas with density ρ, i.e. the exchange-correlation energy is *locally* approximated by the exchange-correlation energy of the homogeneous electron gas which has a uniform density that is equal to ρ. This is valid if the inhomogeneity of $\rho(\mathbf{r})$ is small, but in many materials this is not the case and the LDA is a rather crude approximation. However for many materials LDA gives surprisingly good results even if the inhomogeneity is large. Chaperly and Alder created an interpolation formula for the exchange-correlation energy density of the homogeneous electron gas for any density by numerical simulations of the jellium model [3].

In order to perform spin-polarized calculations to include non-homogeneous spin densities, the Hohenberg-Kohn theorem and the Kohn-Sham equations need to be supplemented with a spin index and in this case the LDA is easily adjusted to the local spin density

approximation (LSDA):

$$E_{xc}^{LSDA}[\rho_\uparrow, \rho_\downarrow] = \int d\mathbf{r}\rho(\mathbf{r})\epsilon_{xc}^{LSDA}(\rho_\uparrow(\mathbf{r}), \rho_\downarrow(\mathbf{r})) \tag{1.10}$$

A typical error of LDA is overbinding. When some of the electrons are well localized in certain orbitals (typically d- and f-orbitals) the participation of those electrons in the electronic cohesive energy of the solid is overestimated. This results in a too small value of the unit cell volume at equilibrium.
Furthermore LDA completely fails for strongly correlated materials that are the scope of this thesis and are discussed in following chapters.

Generalized Gradient Approximation

The generalized gradient approximation (GGA) functional additionally contains the derivative of the density $\rho(\mathbf{r})$:

$$E_{xc}^{GGA}[\rho_\uparrow, \rho_\downarrow] = \int d\mathbf{r}\rho(\mathbf{r})\epsilon_{xc}^{GGA}(\rho_\uparrow(\mathbf{r}), \rho_\downarrow(\mathbf{r}), \nabla\rho_\uparrow(\mathbf{r}), \nabla\rho_\downarrow(\mathbf{r})) \tag{1.11}$$

In many aspects GGA is more accurate than LDA, but does not have a single universal form and depend on a set of adjustable parameters. Common GGA functionals are Perdew-Wang [4] or Perdew-Burke-Enzerhof (PBE) [5].

1.4 Basis sets: (L)APW+lo

In this thesis, the Kohn-Sham wave functions $\psi_{\mathbf{k}\nu}^{\sigma}(\mathbf{r})$ are calculated using the full-potential (linearized) augmented plane-wave ((L)APW) + local orbitals (lo) method as implemented in the electronic structure code WIEN2K [6, 7]. A detailed description of the WIEN2K code can be found in [8]. For the purpose of this thesis we give a short introduction to the used basis set of (L)APW+lo.
It turns out that augmented plane waves (APW) are specially suited as a basis set to solve the Kohn-Sham equations for the effective potential of a crystal. Such a potential varies smoothly in the interstitial region between the atoms and is atomic-like near the atomic nuclei. Therefore the crystal is divided into non-overlapping atomic spheres (muffin-tin

spheres) S^{α}_{MT} around each atom α and the interstitial region I in between the spheres (as seen in Fig. 1.2).

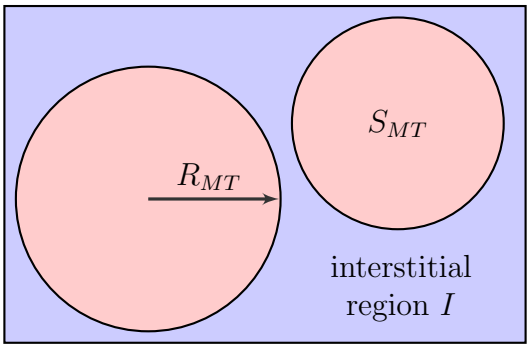

FIGURE 1.2: Partitioning of the unit cell into muffin-tin sphere S^{α}_{MT} with a radii R^{α}_{MT} and an interstitial region I between the spheres.

In the original APW basis the basis functions are energy-dependent which leads to non-linear equations for matching the functions at the sphere boundaries. This complication can be avoided when using *linearized* augmented plane waves (LAPW) [9, 10]. Furthermore to account for semicore bands so called *local orbital* basis functions are used. A local orbital is defined for a particular atom α and particular quantum numbers l and m. In this (L)APW+lo method the eigenfunctions of the Kohn-Sham Hamiltonian are expanded as follows:

$$\psi^{\sigma}_{\mathbf{k}\nu}(\mathbf{r}) = \sum_{\mathbf{K}} c^{\sigma}_{\mathbf{K}\nu}(\mathbf{k})\phi^{\mathbf{k}\sigma}_{\mathbf{K}}(\mathbf{r}) \tag{1.12}$$

with $\mathbf{K}$ the reciprocal lattice vectors, ν the band index and σ the spin degree of freedom. The basis functions $\phi^{\mathbf{k}\sigma}_{\mathbf{K}}(\mathbf{r})$ are now the (L)APW functions. For numerical calculations the total number of basis functions considered is of course limited and therefore the sum over $\mathbf{K}$ is restricted by a maximum value K_{max}. Additional local orbital terms (lo, LO) are added to linearize the basis set and increase its flexibility to describe states of different eigenenergies. In summery any eigenstate of the Kohn-Sham Hamiltonian can be written as:

$$\psi^{\sigma}_{\mathbf{k}\nu}(\mathbf{r}) = \begin{cases} \dfrac{1}{\sqrt{\Omega}} \displaystyle\sum_{\mathbf{K}} c^{\sigma}_{\mathbf{K}\nu}(\mathbf{k}) e^{i(\mathbf{k}+\mathbf{K})\mathbf{r}} & \text{if } \mathbf{r} \in I \\ \displaystyle\sum_{l,m} \Big[A^{\nu\alpha}_{lm}(\mathbf{k},\sigma) u^{\alpha,\sigma}_{l}(r^{\alpha}, E^{\alpha}_{1l}) + B^{\nu\alpha}_{lm}(\mathbf{k},\sigma) \dot{u}^{\alpha,\sigma}_{l}(r^{\alpha}, E^{\alpha}_{1l}) \\ \qquad + C^{\nu\alpha}_{lm}(\mathbf{k},\sigma) u^{\alpha,\sigma}_{l}(r^{\alpha}, E^{\alpha}_{2l}) \Big] Y^{l}_{m}(\hat{\mathbf{r}}^{\alpha}) & \text{if } \mathbf{r} \in S^{\alpha}_{MT} \end{cases} \tag{1.13}$$

with Ω the volume of the unit cell. In the interstitial region (I) a plane wave expansion is used and inside the muffin-tin spheres S^{α}_{MT} a linear combination of radial functions times spherical harmonics $Y^l_m(\hat{\mathbf{r}}^{\alpha})$ is used. This ensures the flexibility to describe free-electron-like states in the interstitial, and atomic-like states near the nuclei. The coefficients A_{lm}, B_{lm}, and C_{lm} are determined by the normalization and boundary conditions at the muffin-tin spheres. Their explicit expression can be found in the literature [8] and depend on the choice of the basis (whether the atom is described in the APW+lo or the LAPW representation with additional LO terms).
WIEN2K is based on a full-potential method, meaning that all electronic shells are used to calculated the Kohn-Sham-potential. In its general form the Kohn-Sham-potential is expanded as,

$$v^{KS}(\mathbf{r}) = \begin{cases} \sum_{\mathbf{K}} v_{\mathbf{K}} e^{i\mathbf{K}\mathbf{r}} & \text{if } \mathbf{r} \in I \\ \sum_{l,m} v_{lm}(\mathbf{r}) Y^l_m(\hat{\mathbf{r}}) & \text{if } \mathbf{r} \in S^{\alpha}_{MT} \end{cases} \tag{1.14}$$

where $\hat{\mathbf{r}}$ indicating the angles θ and φ, which specify the direction of $\mathbf{r}$ in spherical coordinates.

1.5 Limitations of DFT-LDA

Using standard approximations to the exchange-correlation functional, density functional calculations are mainly restricted to materials for which the picture of individual electrons is applicable or the quasi-particles are weakly interacting. There is however a large variety of strongly correlated materials for which this standard approach of electronic structure calculations breaks down. In these materials the electrons can no longer be considered individually and therefore DFT calculations within LDA or GGA lead to a qualitatively wrong result compared to experiments. Well known examples are transition metal oxides or pnictide materials with partially filled d- or f-shells.

The main problem of LDA in capturing strong correlation effects is that the approximations for the exchange-correlation energy are based on the homogeneous electron gas which is not adequate for systems with narrow bands, i.e for materials where the on-site Coulomb interaction is comparable with the band width. The narrower a band the more localized is an electron and the longer it resides on an atom. Therefore it feels the

presence of other electrons. The case of electrons being localized occur when the kinetic energy gain of an electron due to hopping from site to site is smaller than the energy loss due to Coulomb repulsion U between electrons sitting on the same orbital. So for strong Coulomb repulsion U the double occupied orbitals become energetically very expensive and the system may reduce its total energy by localizing the electrons. The Hubbard parameter U defines the strength of the Coulomb repulsion and gives the energy cost to place two electrons in the same orbital. The classical example of this behavior are Mott insulators [11] with partially filled d-shells like transition-metal oxides such as MnO, FeO, CoO and NiO [12]. DFT-LDA give a metallic ground state while experiments show an insulator with a large gap. So strong electronic correlations in these systems require a treatment that goes beyond DFT-LDA. Combing DFT with the model Hamiltonian approach leads to first successful attempts to describe Mott insulators. In particular LDA is combined with a basically static mean field approximation for the remaining part of the U [13, 14]. This LDA+U method takes into account the orbital dependence of the Coulomb and exchange interactions which is absent in the LDA and was found to be very useful in the study of long-range ordered insulating states. However, especially the intermediate region where the electrons are neither perfectly localized nor fully itinerant, requires a treatment that goes beyond a static mean-field approximation and includes dynamical effects. Here the highly promising LDA+DMFT method seems to close the gap by combining electronic band structure calculations and the dynamical mean-field theory. The LDA+DMFT method is the focus of this thesis and will be explained in the next chapters.

Chapter 2

Dynamical Mean Field Theory

2.1 From the lattice to the quantum impurity model

The essential idea in dynamical mean field theory (DMFT) is to map a lattice model with many degrees of freedom onto a self-consistent single-site quantum impurity problem, where a single impurity is coupled to a self-consistently determined non-interacting bath. One of the simplest lattice models of correlated electrons is the Hubbard model:

$$\hat{H} = \sum_{\langle ij \rangle, \sigma} t_{ij} \hat{c}^{\dagger}_{i\sigma} \hat{c}_{j\sigma} + U \sum_{i} \hat{n}_{i\uparrow} \hat{n}_{i\downarrow} \tag{2.1}$$

This model describes electrons with spin directions $\sigma =\uparrow$ or $\downarrow$ moving between localized states at lattice sites i and j. The first term is the kinetic energy, characterized by the hopping term t_{ij}. The second term describes the Coulomb interaction between electrons meeting on the same lattice site i (The Pauli principle requires them having opposite spin).

To understand the basics of DMFT we first consider the Weiss mean-field approximation for classical interacting spins (the Ising model) as an analogy. There the spin at a single site is the relevant degree of freedom and all interactions with other degrees of freedom are merged into an effective magnetic field (the classical mean field or Weiss field). This Weiss field is set such that it reproduces the expectation value of a specific local observable of the lattice model, in the classical case the thermal average of the magnetization. This mean field approximation even becomes exact in the limit of infinite coordination, which appears quite intuitive. When the number of neighbors of a site becomes large they can

be treated globally as an external bath.

This concept can be extended to a *dynamical* mean-field theory in the quantum case like for the Hubbard model. In the quantum case the relevant degrees of freedom are the quantum states of a single site in a lattice. The rest of the lattice is described as a bath of non-interacting electrons. The effect of the bath on the single site is captured by a hybridization function, which describes the ability of electrons to enter or leave the single site and thus allow the site to make transitions between different configurations. So the hybridization function can be seen as the mean-field, however it is now not only a number anymore but a function of frequency and therefore we can call it *dynamical* mean-field. In the single band Hubbard model each site can undergo transitions between the four possible quantum states $|0\rangle$, $|\uparrow\rangle$, $|\downarrow\rangle$ and $|\uparrow\downarrow\rangle$ by exchanging electrons with the bath. The model of a single site coupled to a bath of non-interacting electrons corresponds to the well studied single-site Anderson impurity model (SIAM) [15], that can be solved much easier than the original model by various numerical methods.

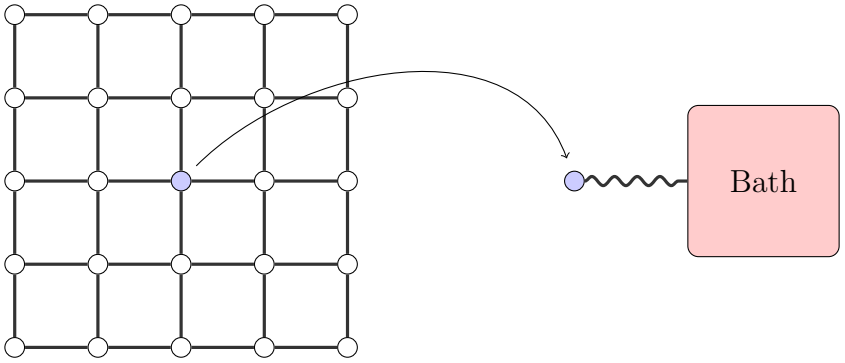

FIGURE 2.1: DMFT replaces the original lattice problem by a single site coupled to a bath.

Within DMFT, the Hamiltonian (2.1) can be mapped onto a SIAM, where $(\hat{d}_\sigma, \hat{d}_\sigma^\dagger)$ are particle operators for an *impurity orbital* and the bath can be seen as a *conduction band* described by $(\hat{a}_{k\sigma}, \hat{a}_{k\sigma}^\dagger)$:

$$\hat{H}_{\mathrm{AIM}} = \underbrace{\sum_{k,\sigma} \epsilon_k \hat{a}_{k\sigma}^\dagger \hat{a}_{k\sigma}}_{\text{free bath states}} + \underbrace{\sum_{k,\sigma} V_k (\hat{a}_{k\sigma}^\dagger \hat{d}_\sigma + \hat{d}_\sigma^\dagger \hat{a}_{k\sigma})}_{\text{hybridization}} + \underbrace{\sum_{\sigma} \epsilon_0 \hat{d}_\sigma^\dagger \hat{d}_\sigma + U \hat{n}_{d\uparrow} \hat{n}_{d\downarrow}}_{\text{local many-body interaction}} \tag{2.2}$$

The first term is the energy of bath with energy levels ϵ_k, the second term describes the hybridization between the bath and the impurity with V_k being the quantum mechanical amplitude for electrons hopping in or out of the impurity site. The third term denotes the energy of the impurity and the last term gives the local Coulomb interaction for

the impurity with particle number operators $\hat{n}_{d\sigma} = hatd^{\dagger}_{\sigma}\hat{d}_{\sigma}$. Note that the Coulomb interaction is considered only locally on the impurity site. The index k is a degree of freedom of the electronic states of the bath. It should be mentioned that the ϵ_k's are effective parameters that should not be confused with the single-particle energies $\epsilon_{\mathbf{q}}$ of the original lattice model ($\epsilon_{\mathbf{q}}$ is the Fourier transform of the hopping amplitude t_{ij}).
We are interested in the dynamics of the impurity orbital and therefore in finding the Greens function of the impurity. In the Feynman path integral representation the Green function of the impurity cab be written as:

$$G_{\text{imp}}(\tau - \tau') = -\langle \hat{T}_{\tau}\hat{d}_{\sigma}(\tau)\hat{d}^{\dagger}_{\sigma}(\tau')\rangle = \frac{1}{Z}\int \mathcal{D}[\hat{d}^{\dagger}_{\sigma}, \hat{d}_{\sigma}]\hat{d}^{\dagger}_{\sigma}(\tau')\hat{d}_{\sigma}(\tau)e^{-S} \tag{2.3}$$

with the imaginary-time action S. Since we are focusing on the dynamics of the impurity orbital and the Hamiltonian is quadratic in the bath operators $(\hat{a}_{k\sigma}, \hat{a}^{\dagger}_{k\sigma})$, the bath degrees of freedom can be integrated out. This leads to the local effective action for the impurity orbital:

$$S_{\text{eff}} = -\sum_{\sigma}\int_0^{\beta} d\tau \int_0^{\beta} d\tau' \hat{d}^{\dagger}_{\sigma}(\tau)\mathcal{G}_0^{-1}(\tau - \tau')\hat{d}_{\sigma}(\tau') + U\int_0^{\beta} d\tau \hat{n}_{d\uparrow}(\tau)\hat{n}_{d\downarrow}(\tau) \tag{2.4}$$

where $\mathcal{G}_0(\tau - \tau')$ is the effective non-interacting bath Green function that can be seen as the bare propagator for an electron created on the impurity at imaginary time τ (coming from the external bath) and destroyed at imaginary time τ' (going back to the bath). It contains all the information about the structure of the bath and is in the literature also refereed to as the Weiss effective field as comparison to the classical model. The Fourier transform of this propagator can be written in the general form

$$\mathcal{G}_0^{-1}(i\omega_n) = i\omega_n - \epsilon_0 + \mu - \Delta(i\omega_n), \tag{2.5}$$

where the hybridization of the impurity orbitals with the effective bath is described by the hybridization function $\Delta(i\omega_n)$

$$\Delta(i\omega_n) = \sum_{\mathbf{k}} \frac{|V_{\mathbf{k}}|^2}{i\omega - \epsilon_{\mathbf{k}} + \mu}. \tag{2.6}$$

It is decisive for the mapping that the hybridization function $\Delta(i\omega_n)$ is chosen such that the impurity model reproduces the exact local Green function of the lattice model. In other words $\mathcal{G}_0(i\omega_n)$ has to be determined such that, when inserted in the Anderson model,

the resulting interacting impurity Greens function $G_{\text{imp}}(i\omega_n)$ obeys a self-consistency condition. This self-consistency condition requires the impurity Green function to coincide with the on-site local Green function of the lattice $G(i\omega_n) = \sum_{\mathbf{k}} G(\mathbf{k}, i\omega_n)$:

$$\boxed{G_{\text{imp}}(i\omega_n) \stackrel{!}{=} G(i\omega_n) = \sum_{\mathbf{k}} G(\mathbf{k}, i\omega_n)} \tag{2.7}$$

If this condition is fulfilled the Hamiltonian (2.2) serves as a reference system for the Hubbard model (2.1). This mapping of a lattice model onto a quantum impurity model is the decisive part of DMFT.

2.2 Dynamical mean-field equations

In order to get all the necessary equations for the whole DMFT procedure we start with the key quantity of DMFT. To study the problem we introduce the one-particle lattice Green function

$$G_{ij}^{\sigma}(\tau - \tau') = -\langle \hat{T}_\tau \hat{c}_{i\sigma}(\tau) \hat{c}_{j\sigma}^{\dagger}(\tau') \rangle \,. \tag{2.8}$$

A Fourier transform and summation over all $\mathbf{k}$-values lead to the local Green function of the lattice as the key quantity of DMFT:

$$G(i\omega_n) = G_{ii}(i\omega_n) = \sum_{\mathbf{k}} G(\mathbf{k}, i\omega_n) = \sum_{\mathbf{k}} \frac{1}{i\omega_n - \epsilon_{\mathbf{k}} + \mu - \Sigma(i\omega_n)} \tag{2.9}$$

where $\omega_n = (2n+1)\pi/\beta$ are the Matsubara frequencies with β the inverse temperature. Again the idea of DMFT is to identify the on-site Green Function of the lattice $G(i\omega_n)$ with the Green function of an effective single impurity model which has the same on-site Coulomb interaction as in the Hubbard model.

$$G^{\sigma}(i\omega_n) = G_{\text{imp}}^{\sigma}(i\omega_n) \tag{2.10}$$

The corresponding impurity model for the Hubbard model is the single impurity Anderson model (2.2). The effective dynamics at the impurity are conveniently described in terms of an imaginary-time action, which takes into account the retardation effects of electrons hopping in and out of the single site.

$$S_{\text{eff}} = -\sum_{\sigma} \int_0^{\beta} d\tau \int_0^{\beta} d\tau' \hat{d}_{\sigma}^{\dagger}(\tau) \mathcal{G}_0^{-1}(\tau - \tau') \hat{d}_{\sigma}(\tau') + U \int_0^{\beta} d\tau \hat{n}_{d\uparrow}(\tau) \hat{n}_{d\downarrow}(\tau) \tag{2.11}$$

Again we like to mention that $\mathcal{G}_0(\tau - \tau')$ is the equivalent to the Weiss effective field in the classic case, with the main difference that it is a function of time (or a function of frequency in the Matsubara representation respectively) instead of a single number. It therefore fully accounts for local quantum fluctuations of the impurity due to the coupling with the bath of electrons. However spatial fluctuations are neglected in this description. Equivalent to the local on-site Green function of the lattice we can introduce the impurity Green function that can be calculated from the effective action:

$$G_{\text{imp}}(\tau - \tau') = -\langle \hat{T}_\tau \hat{d}_\sigma(\tau) \hat{d}^\dagger_\sigma(\tau') \rangle_{S_{\text{eff}}} \tag{2.12}$$

A Fourier transform yields the Matsubara Green function $G_{\text{imp}}(i\omega_n)$:

$$G_{\text{imp}}(i\omega_n) = \int_0^\beta d\tau G_{\text{imp}}(\tau) e^{i\omega_n \tau} \tag{2.13}$$

The non-interacting bath Green function $\mathcal{G}_0(i\omega_n)$ of the SIAM is connected to the local lattice Greens function $G(i\omega_n)$ of the Hubbard model and the impurity self energy $\Sigma_{\text{imp}}(i\omega_n)$ via the Dyson equation (For simplicity we skip the spin index σ from now on.):

$$\mathcal{G}_0^{-1}(i\omega_n) = G^{-1}(i\omega_n) + \Sigma_{\text{imp}}(i\omega_n) \tag{2.14}$$

Solving the impurity model (i.e. solving S_{eff}) defined by the bath Greens function $\mathcal{G}_0(i\omega_n)$ is the main difficulty in the whole process and can be done by various numerical methods we will discuss later. From the solution of the impurity model we are getting $G_{\text{imp}}(i\omega_n)$ and $\Sigma_{\text{imp}}(i\omega_n)$. The *impurity* self-energy is now used as an approximation of the *lattice* self-energy.

$$\Sigma(\mathbf{k}, i\omega_n) \approx \Sigma(i\omega_n) = \Sigma_{\text{imp}}(i\omega_n) \tag{2.15}$$

Considering the lattice self-energy as purely local is the main approximation within the DMFT scheme and allows us to reduce the lattice problem to a quantum impurity model. A local self-energy of the lattice implies that the effective mass, coherence temperature and lifetimes are constant along the Fermi surface. The approximated self-energy is used to determine the local lattice Green function.

$$G(i\omega_n) = \sum_k \frac{1}{i\omega_n - \epsilon_{\mathbf{k}} + \mu - \Sigma_{\text{imp}}(i\omega_n)} \tag{2.16}$$

This equation is used in the self-consistency condition, requiring that the on-site local Green function of the lattice $G(i\omega_n)$ coincides with the impurity Greens function

$G_{\text{imp}}(i\omega_n)$. For more details on DMFT one can refer to the reviews [16, 17, 18].

2.3 The DMFT self-consistent iterative loop

The equations from the previous section can be regarded as system of equations for the unknown functions $\mathcal{G}_0(i\omega_n)$ and $\Sigma_{\text{imp}}(i\omega_n)$. The system is solved iteratively till self-consistency is achieved, where at every iteration the following steps are performed:

1. At first an input value for the self-energy $\Sigma(i\omega_n)$ is set and from this the lattice Green function $G(i\omega_n)$ is calculated with equation (2.9).
2. Form the Dyson equation (2.14) the bath Green function $\mathcal{G}_0(i\omega_n)$ is obtained.
3. The SIAM defined by $\mathcal{G}_0(i\omega_n)$ is solved to get the interacting impurity Green function $G_{\text{imp}}(i\omega_n)$ and the impurity self-energy $\Sigma_{\text{imp}}(i\omega_n)$.
4. The lattice self-energy is approximated by the impurity self-energy and equation (2.16) is used to obtain a new lattice Green function $G(i\omega_n)$, which closes the self-consistent loop.

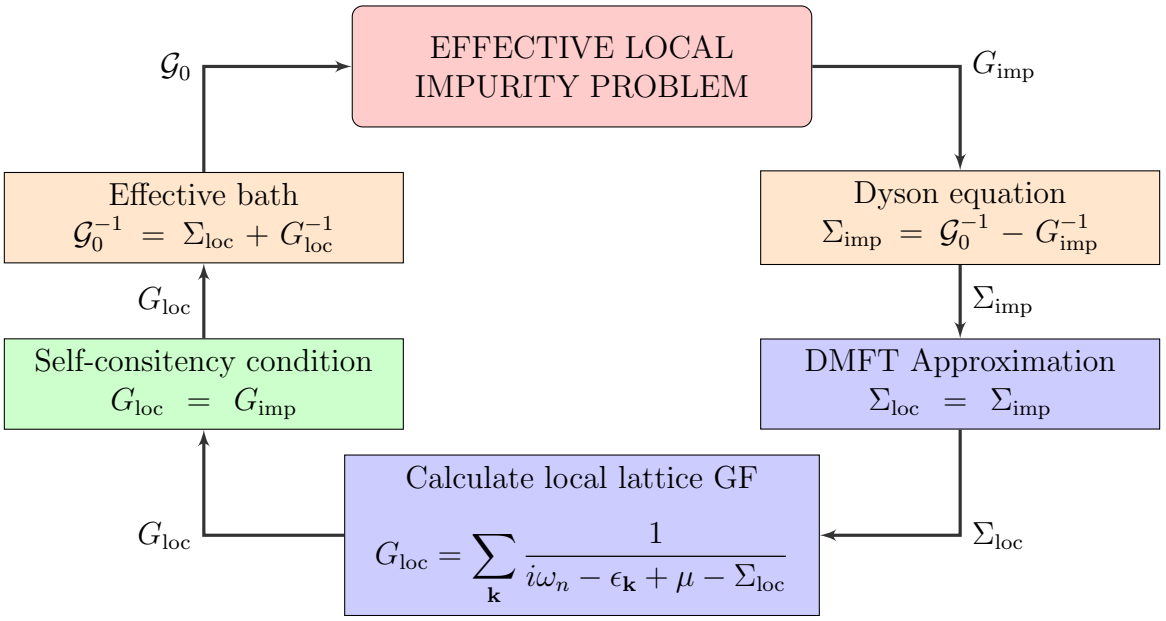

FIGURE 2.2: The DMFT self-consisted iterative loop.

The iteration loop runs until the self-energy $\Sigma(i\omega_n)$ for step 1 will to some accuracy become equal to the output value from step 3. The whole DMFT calculation scheme for the Hubbard model is defined by those steps.

It is worth to note that instead of the non-interacting energy spectrum $\epsilon_{\mathbf{k}}$ of the lattice the corresponding density of states $\rho_0(\epsilon)$ may be used to calculate the local lattice Green function $G(i\omega)$:

$$G(i\omega_n) = \int d\epsilon \frac{\rho_0(\epsilon)}{i\omega_n - \epsilon_0 + \mu - \Sigma(i\omega_n)} \tag{2.17}$$

where the density of states is defined as:

$$\rho_0(\epsilon) = \sum_{\mathbf{k}} \delta(\epsilon - \epsilon_{\mathbf{k}}) \tag{2.18}$$

In our derivation the Green functions are always defined on imaginary Matsubara frequencies $i\omega_n$ like the Green function above. For getting values on the real axis we need to perform an analytical continuation from discrete imaginary frequencies to real frequencies. The procedure for this analytical continuation is described in one of the next sections. From the transformation $i\omega_n \to \omega_n + i\delta$ we obtain the local retarded Green function $G(\omega)$:

$$G(i\omega_n \to \omega + i\delta) = G(\omega) = \Re[G(\omega)] + i\Im[G(\omega)] \tag{2.19}$$

From the local retarded Green or rather from its spectral function $A(\omega)$, all single particle properties of the system can be obtained (e.g. the density of states).

$$A(\omega) = -\frac{1}{\pi}\Im[G(\omega)] \tag{2.20}$$

Rewriting this expression the spectral function can also be calculated from the self energy:

$$A(\omega) = -\frac{1}{\pi}\sum_{\mathbf{k}} \frac{\Im[\Sigma(\omega)]}{(\omega - \epsilon_{\mathbf{k}} + \mu - \Re[\Sigma(\omega)])^2 + \Im[\Sigma(\omega)]^2} \tag{2.21}$$

2.4 Limits in which DMFT becomes exact

DMFT leads to the exact solution in these three simple limits:

1. In the limit of infinite space dimensions $d \to \infty$: This is equivalent to the limit of infinite coordination number z. In this limit the *lattice* self-energy becomes purely local, i.e. does not depend on momentum $\mathbf{k}$ and the DMFT approximation (2.15) becomes exact.

$$\Sigma(\mathbf{k}, i\omega_n) \xrightarrow{d\to\infty} \Sigma(i\omega_n) \quad \text{or} \quad \Sigma_{ij}(i\omega_n) \xrightarrow{d\to\infty} \delta_{ij}\Sigma(i\omega_n) \tag{2.22}$$

k-independence of the self-energy in real space representation means that the matrix $\Sigma_{ij}(i\omega_n)$ becomes diagonal.

2. In the non-interacting limit $U = 0$, the self-energy vanishes. Solving the effective action (2.11) yields $G(i\omega_n) = \mathcal{G}_0(i\omega_n)$ and from the the self-consistency condition, $G(i\omega_n)$ reduces to the non-interacting local Green function making the DMFT approximation exact.

3. In the atomic limit $t_{ij} = 0$, there is no hopping between the sites and the Hubbard model describes a collection of isolated sites. Therefore the lattice self-energy only has on-site components. In the Anderson model the hybridization function $\Delta(i\omega_n)$ vanishes, leading to the problem of an isolated impurity. Since there is no particle exchange with the bath anymore the effective action becomes local in time making the DMFT approximation exact.

Since DMFT is exact in the limits two and three which are the weak and the strong coupling limits, it may be seen as a reasonable approximation also in the intermediate region.

2.5 Solving the single impurity Anderson model

A crucial step within the DMFT scheme is to reliably solve the quantum impurity model. There exists various techniques to solve the SIAM, such as quantum Monte Carlo (QMC) simulations based on the Hirsch-Fly algorithm, numerical renormalization group (NRG) or iterative perturbation theory (IPT). While the Hirsch-Fye algorithm is very popular it has the time discretization as an essential drawback. The discretization can become very large with lowering the temperature leading to a severe discretization error. Recently new continuous-time quantum Monte Carlo (CT-QMC) methods were developed to solve the quantum impurity model without time discretization [19, 20]. Applications of QMC to fermionic lattice problems are limited by a severe sign problem, however, CT-QMC turned out to be a very powerful tool for solving fermionic impurity models where it has a much less severe sign problem or in some cases the sign problem is even absent. In this work only CT-QMC is used in the calculations and will be described in more detail.

Continuous-time quantum Monte Carlo

In general a quantum impurity model may be written as a Hamiltonian consisting of three basic terms:

$$\hat{H}_{\mathrm{QIM}} = \hat{H}_{\mathrm{loc}} + \hat{H}_{\mathrm{bath}} + \hat{H}_{\mathrm{hyb}} \tag{2.23}$$

The impurity $\hat{H}_{\mathrm{loc}}$, usually a system with a rather small number of degrees of freedom described by the operators $(\hat{d}_\sigma, \hat{d}^\dagger_\sigma)$, the non-interacting bath $\hat{H}_{\mathrm{bath}}$ described by $(\hat{a}_\sigma, \hat{a}^\dagger_\sigma)$ and the coupling term between the impurity and the bath $\hat{H}_{\mathrm{hyb}}$.

The main advantage of continuous-time methods is to avoid the regular discretization of the thermodynamic time interval $0 \leq \tau \leq \beta$. This avoids time-discretization allows to treat the problem for arbitrary large β values and therefore to investigate low-temperature regions.
The basic idea is to split the Hamiltonian $H = H_a + H_b$ into two parts and to write the partition function Z in the interaction representation with respect to H_a and expand in powers of H_b.

$$\begin{aligned} Z &= \mathrm{Tr}[T e^{-\beta H_a} e^{-\int_0^\beta d\tau H_b(\tau)}] \\ &= \sum_k \int_0^\beta d\tau_1 \ldots \int_{\tau_{k-1}}^\beta d\tau_k \frac{(-1)^k}{k} \mathrm{Tr}\left[e^{-\beta H_a} H_b(\tau_k) \ldots H_b(\tau_1)\right] \end{aligned} \tag{2.24}$$

Monte Carlo configurations are now represented as segments $\{\tau_i, \tau_j\}$ which continuously fill the imaginary time interval, and τ_i and τ_j are chosen stochastically. There are basically two versions of CT-QMC: The weak-coupling expansion where the expansion of the partition function is done in powers of the interaction term H^I_{loc}, and the hybridization expansion where the expansion is done in powers of the hybridization term H_{hyb}.
In this work we use an implementation of the hybridization expansion based on the segment representation. In this approach, Monte Carlo configurations consist of a sequence of creation and annihilation operators, and thus represent a sequence of hybridization events (electrons hopping from the bath to the impurity or back into the bath). The hybridization expansion approach is particularly well suited for the multi-orbital impurity problems that typically appear in LDA+DMFT calculations. The advantage is that arbitrary complicated impurity interactions can be treated, although the number of orbitals is limited by the exponential growth of the local Hilbert space. For further details we refer the reader to [21].

Real materials and interactions

For real material calculations, impurity models with more degrees of freedom are used. This is because of a more complicated structure of the interactions, therefore we need more degrees of freedom to describe the richer variety of physical phenomena. For example in our case, where we study transition metal materials with partially filled d-shells, not only the density-density Coulomb interaction but also the Hund's rule physics is relevant for an adequate description of these materials. The Hund's rule says that configurations with maximal spin and orbital angular momentum are preferred.
The interaction Hamiltonian to describe different configurations of electrons in the d-orbitals of the studied materials in general consists of 2-particle terms like $U_{ijkl}\hat{c}_i^\dagger\hat{c}_j^\dagger\hat{c}_l\hat{c}_k$:

$$\hat{H}_{loc} = \sum_{ijkl} U_{ijkl}\hat{c}_i^\dagger\hat{c}_j^\dagger\hat{c}_l\hat{c}_k \tag{2.25}$$

U_{ijkl} are the screened Coulomb matrix elements. For d-electrons this interaction matrix elements are typically expressed in terms of the three Slater integrals F_0, F_2 and F_4 with $U = F_0$ (direct Coulomb interaction, Hubbard U) and $J = \frac{1}{14}(F_2 + F_4)$ (exchange Coulomb interaction, Hund's exchange J). The third parameter is set by the atomic ratio $\frac{F_4}{F_2} = 0.625$.
In practice, however, often only density-density interactions $U_{mm'}\hat{n}_m(\mathbf{r})\hat{n}_{m'}(\mathbf{r})$ are taken into account because of technical reasons when using QMC solvers. In this case the configuration can be represented by the segment picture [20] which is numerically more efficient and therefore much faster.
Furthermore the definition of the Hubbard U and Hund's exchange J is a crucial task. One needs to consider screening effects that play a major role in real materials. Starting from a huge unscreened value (e.g. $U = 10 - 20$ eV) the effective value may be much smaller ($U \sim 4$ eV) due to screening effects.

2.6 Maximum entropy method

Since QMC is formulated in imaginary time τ and discrete imaginary Matsubara frequencies $i\omega_n$, dynamical information (e.g. the spectral function $A(\omega)$) on the real axis can only be obtained from analytic continuation of the QMC data. In particular we need to perform an analytical continuation of the Green function $G(i\omega_n)$ or the self energy

$\Sigma(i\omega_n)$. The spectral function on the real axis is linked to the imaginary time Green function via:

$$G(i\omega_n) = \int_{-\infty}^{\infty} d\omega' \frac{A(\omega')}{i\omega_n - \omega'} \qquad G(\tau) = \int_{-\infty}^{\infty} d\omega \frac{e^{-\tau\omega}}{1 + e^{-\beta\omega}} A(\omega) \tag{2.26}$$

In the QMC simulations the Green function $G(i\omega_n)$ is measured and may deviate from the exact Green function by statistical and systematic errors. In principle we need to invert the spectral representation of $G(i\omega_n)$ to obtain $A(\omega)$, however, this inversion is ill-conditioned. This is because the fermion kernel $K(\tau, \omega) = \frac{e^{-\tau\omega}}{1+e^{-\beta\omega}}$ becomes exponentially small at large frequencies. Therefore small changes of the Green function in this frequency region may have a huge effect on $A(\omega)$. Hence, from QMC data $G(i\omega_n)$ the spectral function $A(\omega)$ can be calculated accurately only for small frequencies and there exists an infinite number of spectral functions that fulfill Eq. (2.26).
In this work a stochastic maximum entropy method is used to do the analytical continuation. This *MaxEnt* method is based on the Bayesian statistics and finds the most probable solution out of all possible solutions that are consistent with the QMC data. For further details on *MaxEnt* we refer the reader to [22].

Chapter 3

Charge Self-Consistent LDA+DMFT

3.1 Merging conventional band structure calculations with DMFT

To be able to correctly describe the electronic structure of strongly correlated materials a method has been developed that combines density functional theory, mainly in its local density approximation (LDA), and dynamical mean-field theory (DMFT). This LDA+DMFT method [18, 23, 24, 25] includes the advantages of the LDA, which gives a good *ab-initio* description for weakly correlated materials, with the correct treatment of the local correlations within DMFT. The basic idea is to divide the electrons in the material into two groups [26]: weakly correlated electrons (i.e. electrons in s- and p-orbitals) that are well described in the local-density approximation (LDA), and strongly correlated (or more localized) electrons (i.e. d- and f-orbitals) well described using DMFT. The model Hamiltonian for the DMFT is then constructed for the correlated subset $\mathcal{C}$. The next step is to find a suitable basis set for the correlated subspace $\mathcal{C}$. Since DMFT includes local correlations, a local basis set is needed. Wannier functions as introduced in Ref. [27] are an adequate choice for such a basis.

The full-orbital Kohn-Sham Hamiltonian from LDA is then projected onto the correlated subspace of the partially filled orbitals. To this Hamiltonian $\hat{H}_{\mathrm{KS}}$ we add many-body terms $\hat{H}_{\mathrm{U}}$ for the on-site Coulomb interaction U and Hund's coupling J, which act only on the subset of correlated orbitals. Since some correlations are already included in the LDA treatment we further need to subtract a double counting correction $\hat{H}_{\mathrm{DC}}$. Finally

we obtain a model Hamiltonian of the form:

$$\hat{H} = \underbrace{\hat{H}_{\mathrm{KS}} - \hat{H}_{\mathrm{DC}}}_{\text{one-electron Hamiltonian } H_0} + \hat{H}_{\mathrm{U}} \tag{3.1}$$

This model Hamiltonian is then treated within DMFT. The self-consistency in this scheme includes two iteration loops, one for the LDA and the other for the DMFT. We can either perform this loops simply one after another (single-shot calculation, see Fig. 3.1) or we can use a total charge self-consistent scheme where we also start from a converged LDA calculation, but after every DMFT loop we calculate the local density $\rho(\mathbf{r})$ from the full Green function in the local basis and use this density as a new starting point for a LDA cycle until a converged local density is also reached. Only this second scheme is fully self-consistent.

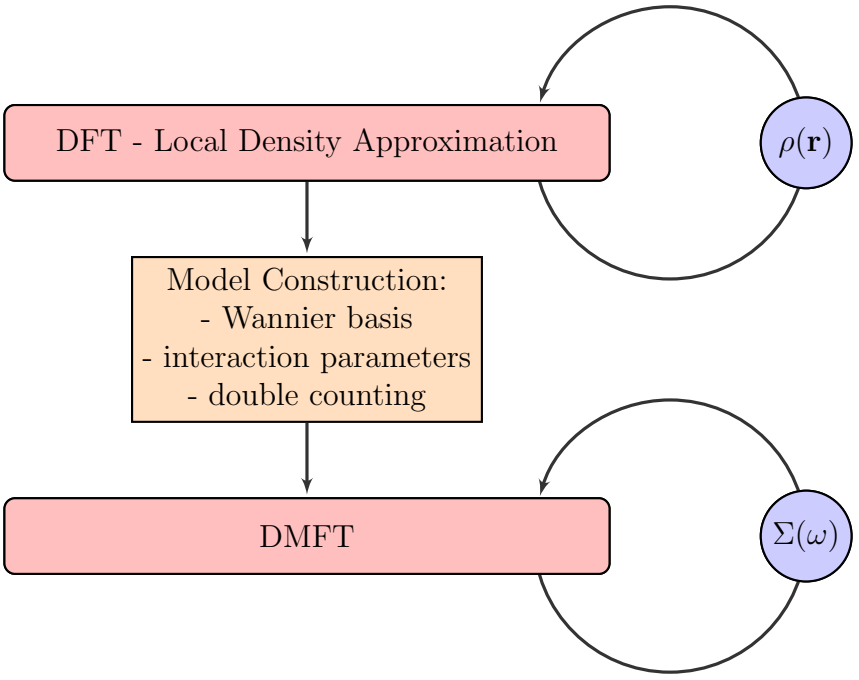

FIGURE 3.1: Flow chart of a single-shot LDA+DMFT calculation. Two separate self-consistent loops over the charge density $\rho(\mathbf{r})$ and the self-energy $\Sigma(\omega)$ are involved.

3.2 Projection onto the correlated subspace

In this thesis we use a projection procedure on Wannier functions within the (L)APW+lo framework introduced in [27]. For this procedure we start from a set of orthonormal local orbitals $|\chi_m^{\alpha\sigma}\rangle$ defined in the unit cell, where α specifies the atom in the unit cell, m is

an orbital index of the correlated subspace, and σ is the spin degree of freedom. These orbitals are then expanded over the Bloch basis set $|\psi^{\sigma}_{\mathbf{k}\nu}\rangle$ which is an output of the electronic structure calculation and is used to describe lattice quantities:

$$|\tilde{\chi}^{\alpha\sigma}_{\mathbf{k}m}\rangle = \sum_{\nu} \langle \psi^{\sigma}_{\mathbf{k}\nu} \,|\, \chi^{\alpha\sigma}_{m} \rangle \, |\psi^{\sigma}_{\mathbf{k}\nu}\rangle \tag{3.2}$$

This leads to a complete basis when the sum runs over all Bloch states of the system. But since we are only interested in a basis for the correlated subspace we need to truncate the expansion. Therefore one first has to define a suitable energy window $\mathcal{W} = [\epsilon_1, \epsilon_2]$ for the relevant Bloch states. The choice of the energy window is an important issue, because it determines the shape and the degree of localization of the Wannier functions. In general the more bands are included the more localized the Wannier functions become. To capture hybridization effects of the correlated orbitals with other states, e.g. the Mn-*d*- with the As-*p*-orbitals in $BaMn_2As_2$, one should take a lager energy window that also contains the Bloch states of the uncorrelated *p*-orbitals. Therefore the energy window $\mathcal{W}$ is often chosen to be larger and the dimension of the Kohn-Sham Hamiltonian used in LDA+DMFT exceeds that of the correlated subspace $\mathcal{C}$. After finding a suitable energy window $\mathcal{W}$ the summation in 3.2 is then restricted to Bloch states inside this energy window.

$$|\tilde{\chi}^{\alpha\sigma}_{\mathbf{k}m}\rangle = \sum_{\nu \in \mathcal{W}} \langle \psi^{\sigma}_{\mathbf{k}\nu} \,|\, \chi^{\alpha\sigma}_{m} \rangle \, |\psi^{\sigma}_{\mathbf{k}\nu}\rangle \tag{3.3}$$

The number of included bands will in general depend on $\mathbf{k}$ and σ. However, due to the truncation the reduced Bloch basis used in the summation is not complete anymore. As a result the set of orbitals $|\tilde{\chi}^{\alpha\sigma}_{\mathbf{k}m}\rangle$ is not orthonormal. To finally get a set of orthonormal Wannier functions we need to perform a Löwdin orthonormalization of the Wannier-like functions $|\tilde{\chi}^{\alpha\sigma}_{\mathbf{k}m}\rangle$:

$$|w^{\alpha\sigma}_{\mathbf{k}m}\rangle = \sum_{\alpha' m'} S^{\alpha\alpha'}_{mm'} \left| \tilde{\chi}^{\alpha'\sigma}_{\mathbf{k}m'} \right\rangle \tag{3.4}$$

Now we have a full orthogonal basis set and can denote the projection operator for the Wannier functions:

$$P^{\alpha\sigma}_{\mathbf{k}} = \sum_{m \in \mathcal{C}} |w^{\alpha\sigma}_{\mathbf{k}m}\rangle \, \langle w^{\alpha\sigma}_{\mathbf{k}m}| \tag{3.5}$$

The matrix elements of the projection operator connecting the Bloch basis with the Wannier basis reads as

$$P^{\alpha\sigma}_{m\nu}(\mathbf{k}) = \langle w^{\alpha\sigma}_{\mathbf{k}m} \,|\, \psi^{\sigma}_{\mathbf{k}\nu} \rangle \,. \tag{3.6}$$

3.3 The LDA+DMFT equations

The DMFT equations have to be solved iteratively. The multi-orbital impurity problem as the most challenging part is defined for the correlated subspace $\mathcal{C}$ by the bath Green function $\mathcal{G}^0$ and the local interaction parameters U and J. Assuming we have already solved the Kohn-Sham problem we can construct the Kohn-Sham Green function as

$$G^{\mathrm{KS}}_{\nu\nu'}(\mathbf{k}, i\omega_n) = \frac{\delta_{\nu\nu'}}{i\omega_n + \mu - \epsilon_{\mathbf{k}\nu}}. \tag{3.7}$$

As initial guess for the bath Green function $\mathcal{G}^0$ the projection of the KS Green function on the correlated subspace is used (for simplicity we omit the indices α and σ in this part),

$$\mathcal{G}^0_{mm'}(i\omega_n) = \sum_{\mathbf{k},\nu\nu'} P_{m\nu}(\mathbf{k}) G^{\mathrm{KS}}_{\nu\nu'}(\mathbf{k}, i\omega_n) P^*_{\nu' m'}(\mathbf{k}), \tag{3.8}$$

which, together with H_{loc}, defines the multi-orbital impurity problem. The solution of the impurity model leads to the impurity Green function $G^{\mathrm{imp}}_{mm'}(i\omega_n)$. The impurity self-energy $\Sigma^{\mathrm{imp}}_{mm'}(i\omega_n)$ is obtained via the Dyson equation:

$$\Sigma^{\mathrm{imp}}_{mm'}(i\omega_n) = [\mathcal{G}^0(i\omega_n)]^{-1}_{mm'} - [G^{\mathrm{imp}}(i\omega_n)]^{-1}_{mm'} \tag{3.9}$$

In the DMFT Approximation the lattice self-energy $\Sigma(\mathbf{k}, i\omega_n)$ for the correlated states is approximated by the impurity self-energy, which relates the impurity model to the lattice. Therefore we upfold the impurity self-energy into the Bloch basis that is used as the complete basis of the problem.

$$\Sigma_{\nu\nu'}(\mathbf{k}, i\omega_n) = \sum_{\alpha,mm'} P^*_{\nu m}(\mathbf{k}) [\Delta\Sigma^{\mathrm{imp}}_{mm'}(i\omega_n)] P_{m'\nu'}(\mathbf{k}) \tag{3.10}$$

where $\Delta\Sigma^{\mathrm{imp}}_{mm'}(i\omega_n) = \Sigma^{\mathrm{imp}}_{mm'}(i\omega_n) - \Sigma^{\mathrm{dc}}_{mm'}(i\omega_n)$. At this step we subtracted the double-counting correction that will be discussed later. The lattice self-energy is now used to

calculate the lattice Green function of the solid in the Bloch basis:

$$[G(\mathbf{k}, i\omega_n)]^{-1}_{\nu\nu'} = (i\omega_n + \mu - \epsilon_{\mathbf{k}\nu})\delta_{\nu\nu'} - \Sigma_{\nu\nu'}(\mathbf{k}, i\omega_n) \tag{3.11}$$

From that we obtain the local Green function by projecting the lattice GF to a set of correlated orbitals m of the correlated atom α and summing over the full Brillouin zone.

$$G^{\mathrm{loc}}_{mm'}(i\omega_n) = \sum_{\mathbf{k},\nu\nu'} P_{m\nu}(\mathbf{k}) G_{\nu\nu'}(\mathbf{k}, i\omega_n) P^*_{\nu' m'}(\mathbf{k}) \tag{3.12}$$

The DMFT self-consistency condition requires that the local Green function of the lattice coincides with the impurity Green function

$$G^{\mathrm{loc}}_{mm'}(i\omega_n) = G^{\mathrm{imp}}_{mm'}(i\omega_n) \tag{3.13}$$

A new bath Green function $\mathcal{G}^0$ for the impurity model is constructed from the Dyson equation:

$$[\mathcal{G}^0(i\omega_n)]^{-1}_{mm'} = \Sigma^{\mathrm{imp}}_{mm'}(i\omega_n) + [G^{\mathrm{loc}}(i\omega_n)]^{-1}_{mm'} \tag{3.14}$$

which closes the DMFT loop.

Charge density update

Due to charge transfer between bands treated within DMFT, also the the chemical potential may be shifted. In particular the real part of the self energy is an effective contribution to the chemical potential. That means that at fixed chemical potential there would be a change of electron count. Therefore we need to adjust the chemical potential such that the resulting charge density ρ_{DMFT} holds the correct total number of electrons N
Correlation effects treated within DMFT therefore also affect the local electronic density. In a complete implementation, self-consistency over the charge density used in LDA should also be reached. Within such an implementation the charge densities that emerge from LDA ρ_{LDA} and from DMFT ρ_{DMFT} are combined to one self-consistently determined charge density $\rho_{LDA+DMFT}$. In this manner, self-energy effects that occur due to DMFT can be coupled back onto the LDA calculation and thus onto bands outside of the correlated subspace.
The local density ρ_{DMFT} for the energy window $\mathcal{W}$ can be calculated from the full lattice

Green function $G_{\nu\nu'}(\mathbf{k}, i\omega_n)$ via the density matrix $N^{\mathbf{k}}_{\nu\nu'}$:

$$N^{\mathbf{k}}_{\nu\nu'} = \sum_n G_{\nu\nu'}(\mathbf{k}, i\omega_n) e^{i\omega_n 0^+} \tag{3.15}$$

$$\rho_{\mathrm{DMFT}}(\mathbf{r}) = \sum_{\mathbf{k},\nu\nu'} \langle \mathbf{r} \,|\, \psi_{\mathbf{k}\nu} \rangle \, N^{\mathbf{k}}_{\nu\nu'} \, \langle \psi_{\mathbf{k}\nu'} \,|\, \mathbf{r} \rangle \tag{3.16}$$

where $\psi_{\mathbf{k}\nu}$ are the KS eigenstates within the energy window $\mathcal{W}$. The total electronic density is obtained from the contributions inside and outside the energy window:

$$\rho(\mathbf{r}) = \rho_{\mathrm{DMFT}}(\mathbf{r}) + \rho_{\mathrm{LDA}}(\mathbf{r}) \tag{3.17}$$

From the charge density a new Kohn-Sham potential $v^{KS}[\rho(\mathbf{r})]$ can be calculated starting a new cycle in a fully charge self-consistent implementation. One of the main advantages of the charge self-consistency is the possibility to calculate the total energies in the formalism. Although the total energy is a natural output quantity of DFT, the one-shot LDA+DMFT post-processing schemes have no direct access to it. The importance of charge self-consistency was shown e.g. for an accurate calculation of the total energy in [28]. The general structure of DMFT with LDA as well as the iterative procedure used in practice is summarized in Fig. 3.2.

3.4 Double-counting corrections

A problem in the construction of the model Hamiltonian for DMFT from LDA is that LDA already takes into account a significant part of the electronic correlations that is again included in explicit many-body methods. Therefore this *double-counting* has to be corrected for LDA+DMFT calculations. However, since DFT itself is not an orbital-resolved theory and LDA is not a well-controlled approximation, an exact formulation of this double-counting correction does not exist. All double counting schemes basically subtract an averaged energy for the occupation of a selected reference state depending only on N^{σ}. Here the two most common approximations, which are the *around mean field* (AMF) and the *full localized limit* (FLL), are introduced.

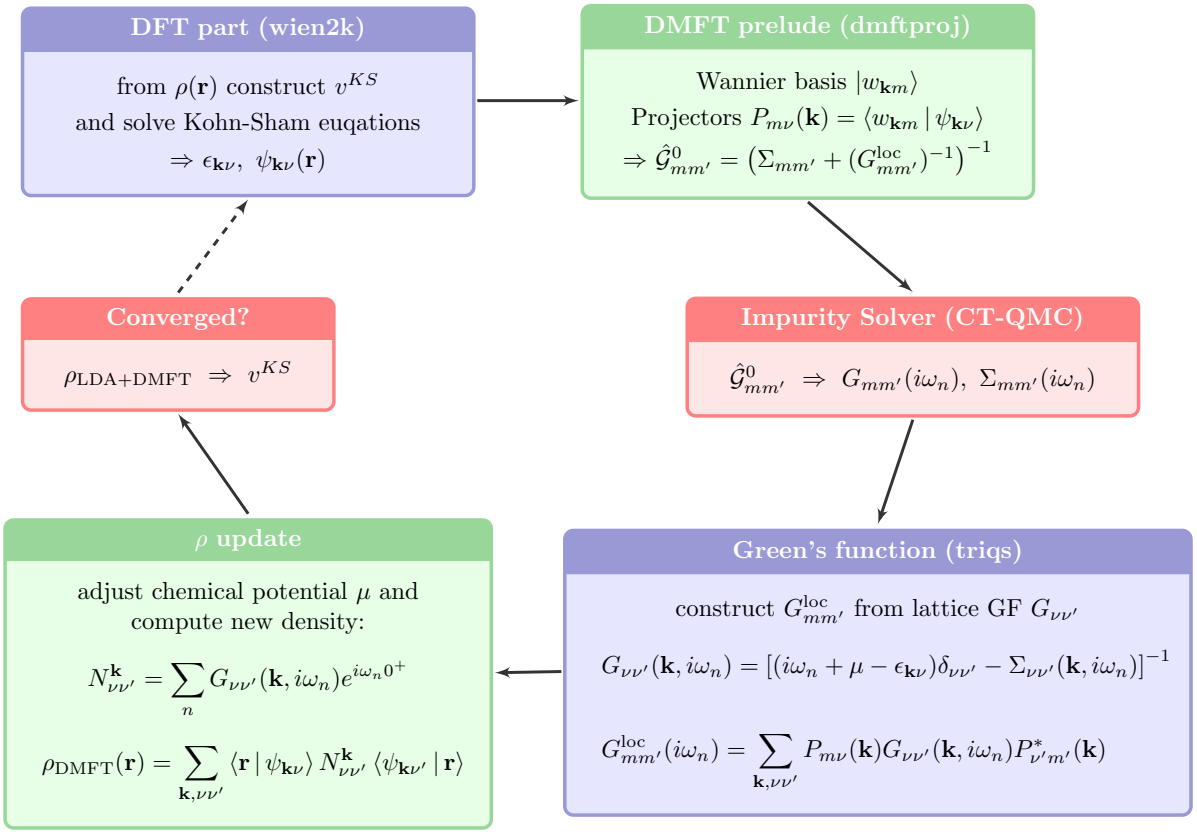

FIGURE 3.2: Flow chart of the LDA+DMFT charge self-consistent scheme.

Fully Localised Limit (FLL)

The fully localised limit (FLL) [29] was originally developed for the LDA+U method. It is argued that the LDA contribution acts on the correlated shell in the form of an electrostatic energy. The idea of the FLL is now that the LDA solution corresponds to the fully localised solution of the Hubbard model. Thus, the FLL is often used for insulating systems close to the atomic limit.

$$E^{\rm dc}_{\rm FLL} = \frac{U}{2} N(N-1) - \frac{J}{2} \sum_\sigma N_\sigma (N_\sigma - 1) \tag{3.18}$$

where N is the total electronic charge of the impurity problem with $N = N^\uparrow + N^\downarrow$. The corresponding potential reads:

$$\Sigma^{\rm dc}_{mm'} = \left[U(N - \frac{1}{2}) - J(N_\sigma - \frac{1}{2}) \right] \delta_{mm'} \tag{3.19}$$

Around Mean Field (AMF)

A similar idea has lead to the around mean field (AMF) approximation [29] which also originates from LDA+U. Here it is assumed that LDA corresponds to a solution in which the occupation numbers are orbital-independent, and thus an orbital-averaged value is used. With the total number of $2l+1$ orbitals per atom we get:

$$E_{\mathrm{AMF}}^{\mathrm{dc}} = \frac{U}{2}N^2 - \frac{1}{2l+1}\left(\frac{U}{2} + lJ\right)\sum_{\sigma} N_{\sigma}^2 \tag{3.20}$$

For the corresponding potential we get:

$$\Sigma_{mm'}^{\mathrm{dc}} = \Big[U(N - \langle n_{\sigma}\rangle) - J(N_{\sigma} - \langle n_{\sigma}\rangle)\Big]\delta_{mm'} \tag{3.21}$$

where $\langle n^{\sigma}\rangle$ is the average electron density per spin and orbital, i.e. 0.5 for a half-filled system. In general AFM is better suited for metals. The difference between AMF and FLL vanishes for half-filled systems and takes its maximum value of $U-J$ for a completely filled or completely empty system.

In our formalism we treat the DC correction on the level of the self energy. The real part of the self energy acts as a contribution to the chemical potential which itself is determined by the number of electrons in the system. After every DMFT loop the chemical potential is set such that the system holds the correct number of electrons. So the DC correction results in an energy shift of the spectrum of the correlated orbitals relative to all other bands. It is important to note that the DC correlation acts on the correlated orbitals only which in the case of manganese pnictides are the Mn-3d bands.

3.5 LDA+DMFT output

The basis output from LDA+DMFT is the self-energy $\Sigma_{mm'}(i\omega_n)$ and the Green function $G_{mm'}(i\omega_n)$ of the correlated subspace. As in Eq. (3.10) the self-energy matrix $\Sigma_{mm'}(i\omega_n)$ can be upfolded to a self-energy in the full Hilbert space $\Sigma_{\nu\nu'}(\mathbf{k}, i\omega_n)$, since the projection matrix between the full orbital basis set and the reduced Wannier basis retains all information on the orbitals below and above the projected energy window. From the self-energy in the full Hilbert space $\Sigma_{\nu\nu'}(\mathbf{k}, i\omega_n)$ one can calculate the full orbital Green

function $G_{\nu\nu'}(\mathbf{k}, i\omega_n)$. However, since we are interested in observable quantities an analytical continuation onto the real frequency axis has to be done. In this work we use the maximum entropy method to perform the transformation: $i\omega_n \to \omega + i\delta$. The maximum entropy method is introduced in chapter 2.6. From *MaxEnt* the real frequency Green function is obtained and one can calculate the **k**-resolved spectral function $A(\mathbf{k}, \omega)$ (as well as the **k**-integrated spectral function $A(\omega)$):

$$A(\mathbf{k}, \omega) = -\frac{1}{\pi}\Im\mathrm{Tr}[G(\mathbf{k}, \omega + i\delta)] \tag{3.22}$$

The spectral function contains the full information about the system and combines the weakly interacting orbitals (s- and p-orbitals) calculated with LDA and the strongly correlated orbitals (e.g., d-orbitals) computed with LDA+DMFT.

Part II

Applications

Chapter 4

$BaMn_2As_2$

4.1 Introduction and crystal structure

The recent discovery of high-temperature superconductivity in the ironbased pnictides, e.g. LaOFeAs [30] and $BaFe_2As_2$ [31, 32, 33], has led to a a lot of experimental and theoretical work with the goal of a better understanding of the properties in these materials. This thesis is aimed at manganese-based compounds with crystal structures similar to the iron-based pnictide superconductors. At first we are focusing on the interesting $BaMn_2As_2$ compound that crystallizes in the tetragonal *I4/mmm* ($ThCr_2Si_2$-type) structure, shown in Fig. 4.1, and is isostructural to $BaFe_2As_2$ (parent compound of the 122 iron arsenide family). The crystal structure in this material is built from charged $[Ba]^{\delta+}$ layers alternating with $[MnAs]^{\delta-}$ layers. The Mn ions form a square lattice sandwiched between two shifted As sheets. Experiments show that $BaMn_2As_2$ is an antiferromagnetic (AFM) insulator with a small band gap, while $BaFe_2As_2$ is an antiferromagnetic metal at low temperatures [34]. $BaMn_2As_2$ is therefore unique compared to the other BaX_2As_2 (X =Fe or Cr) compounds which are all metals. From neutron diffraction measurements the AFM ground state of $BaMn_2As_2$ was found to be of a Néel type (*G-type*) with an ordering temperature of $T_N = 625$ K and an ordered magnetic moment of $\mu = 3.9\ \mu_B$/Mn (at 10 K) oriented along the c axis [35] where μ_B is the Bohr magneton. In contrast, the metallic ground state of $BaFe_2As_2$ is of a *stripe* AFM order below $T_N = 140$ K with a magnetic moment of $\mu = 0.9\ \mu_B$/Fe [36, 37]. Furthermore the magnetic phase transition in $BaFe_2As_2$ coincides with a tetragonal to orthorhombic structural distortion that is driven by magnetic interactions.

The ordered magnetic moment per Mn and the Néel temperature of $BaMn_2As_2$ is substantially larger than of the isostructural compound $BaFe_2As_2$ leading to drastically different properties although Mn ($[Ar]4s^23d^5$) and Fe ($[Ar]4s^23d^6$) are lying next to each other in the periodic system and from a conventional band structure point of view have similar electronic properties (Mn has one electron less than Fe).

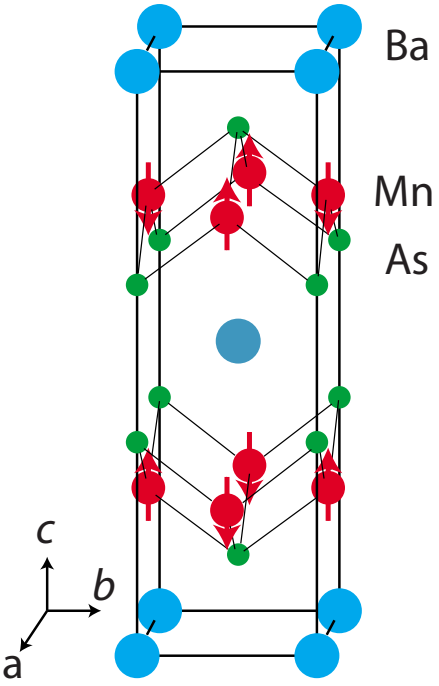

FIGURE 4.1: Crystal and magnetic structure of $BaMn_2As_2$ with *I4/mmm* space group symmetry. The arrows on the Mn atoms represent the *G-type* arrangement of the Mn^{2+} spins in the antiferromagnetically ordered state.

In $BaFe_2As_2$ superconductivity is achieved by electron or hole doping at the Ba site [31], by in-plane doping at the Fe site [32] or by the application of external pressure [33]. Superconductivity in this $BaFe_2As_2$ based compounds coincides with the disappearance of the coupled antiferromagnetic and structural transition, therefore is is thought that spin fluctuations of Fe are important for developing a superconducting ground state. If the structural and magnetic phase transition is successfully suppressed by e.g. doping, superconductivity can be found.

From these promising results it was suggested that doping of $BaMn_2As_2$ can also lead to the development of a unconventional superconducting ground state at high T_C by inducing large antiferromagnetic fluctuations. A lot of effort was made and several transition metals were doped at the Mn site, but it turned out that chemical doping does not have a decisive influence on the long-ranged AFM order in these Mn-based compounds. However, achievements were made in turning $BaMn_2As_2$ metallic by applying high pressure [38] or

by hole doping at the Ba-site [39] leading to a antiferromagnetic local-moment metal. All these unique properties of $BaMn_2As_2$ makes it particularly interesting for further investigations. The goal of this thesis is to better understand the importance of the electronic correlations within the Mn-*d* shells on the band structure, using a fully charge self-consistent LDA+DMFT approach.

	$BaMn_2As_2$	$BaFe_2As_2$
ground state	insulating	metallic
Néel temperature	625 K	140 K
magnetic moment	3.9 μ_B/Mn	0.9 μ_B/Fe

TABLE 4.1: Experimental results for $BaMn_2As_2$ [35] and $BaFe_2As_2$ [36, 37]

4.2 *ab initio* DFT calculations

We are starting with some investigations using conventional band structure calculations within a full-potential (linearized) augmented plane-wave ((L)APW) + local orbitals (lo) implementation (WIEN2K [6]). For the calculations the local density approximation (LDA) and the generalized gradient approximation (GGA) are used. The lattice parameters $a = 4.1684$ Å, $c = 13.4681$ Å with internal parameters $z_{As} = 0.3611$ for $BaMn_2As_2$ [35], and $a = 3.9570$ Å, $c = 12.9685$ Å and $z_{As} = 0.3541$ for $BaFe_2As_2$ [36] are taken from the literature.

4.2.1 Ground state

We begin the discussion of the density functional investigation with the determination of the ground state and a structure optimization for the two compounds $BaMn_2As_2$ and $BaFe_2As_2$. Therefore the total energy was calculated for three cases, the non-spin-polarized case and the two possible antiferromagnetic orderings, *G-type* and *stripe*. Furthermore the total energy calculations were performed for various unit cell volumes, i.e. different lattice parameters. Finally the total energy was plotted against the relative deviation from the unit cell volume calculated form the experimental lattice parameters. The minimum of the total energy was determined by fitting the data to the Birch-Murnaghan

equation of state [40]:

$$E(V) = E_0 + \frac{9V_0B_0}{16}\left\{\left[\left(\frac{V_0}{V}\right)^{\frac{2}{3}} - 1\right]^3 B_0' + \left[\left(\frac{V_0}{V}\right)^{\frac{2}{3}} - 1\right]^2 \left[6 - 4\left(\frac{V_0}{V}\right)^{\frac{2}{3}}\right]\right\} \quad (4.1)$$

where V_0 is the reference volume, V is the deformed volume, B_0 is the bulk modulus, and B_0' is the derivative of the bulk modulus with respect to pressure. The result of the fit is plotted in 4.2. The most stable ground state is the one with the lowest energy.

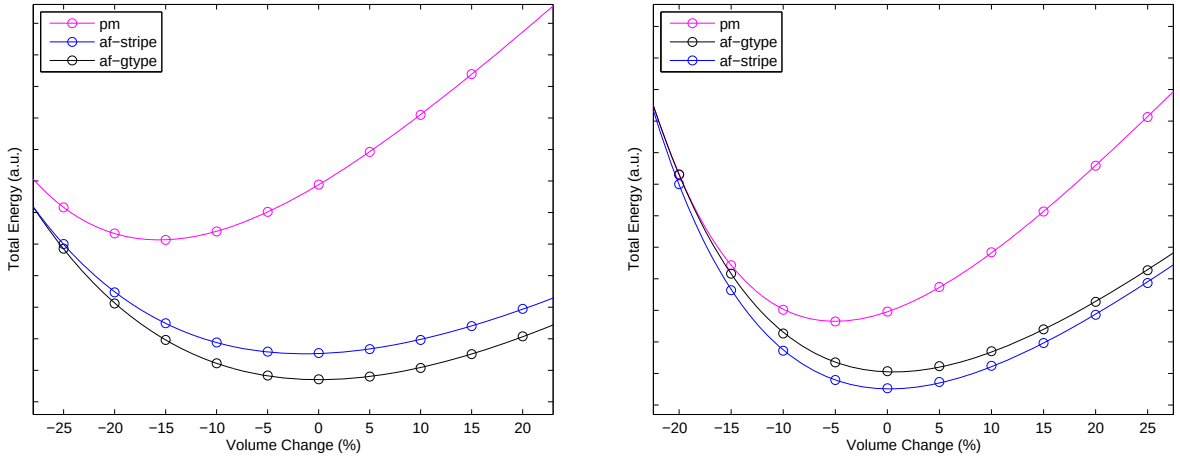

(a) Ba**Mn**$_2$As$_2$ (b) Ba**Fe**$_2$As$_2$

FIGURE 4.2: Volume optimization for paramagnetic and antiferromagnetic $BaMn_2As_2$ and $BaFe_2As_2$, fitted with the Birch-Murnaghan equation of state [40]. Zero denotes the unit cell volume from the experimental lattice parameters. The ground state of both materials is antiferromagetic but in different magnetic orders. We find *G-type* order in $BaMn_2As_2$ whereas the ground state of $BaFe_2As_2$ is of the *stripe-type*

.

The calculations confirm that the *G-type* antiferromagnetic state is the most stable ground state for $BaMn_2As_2$, whereas the *stripe-type* state is the ground state of $BaFe_2As_2$. So already DFT reproduces the experimental ground states for both materials [35, 36]. Also it can be seen that the non-spin-polarized case in general leads to smaller lattice parameters than the antiferromagnetic cases. Underestimation of lattice parameters is typical for LDA calculations (overbinding).

We like to give some more comments on the different antiferromagnetic orderings in the two compounds. Again in the $BaFe_2As_2$ compound, the AFM structure was found to be a *stripe* structure (a schematic representation of the structure can be found in fig. 4.3). In this ordering the spin of the nearest-neighbor (NN) is parallel along one basal-plane axis (the stripe direction) and antiparallel along the other direction. Theoretically it was

shown that within a local moment Heisenberg interaction picture this structure is stabilized if the the AFM next-nearest-neighbor (NNN) interaction J_2 is larger than half the NN interaction J_1 ($J_2 > J_1/2$).
On the other hand, in the *G-type* magnetic structure as observed for $BaMn_2As_2$ all NN spins are antiferromagnetically aligned. Within a local moment picture this already occurs with NN interactions only, not requiring any NNN interactions. The different magnetic structures might indicate that NN interactions are dominant in $BaMn_2As_2$, whereas NNN interactions are important in the tetragonal phase of $BaFe_2As_2$.

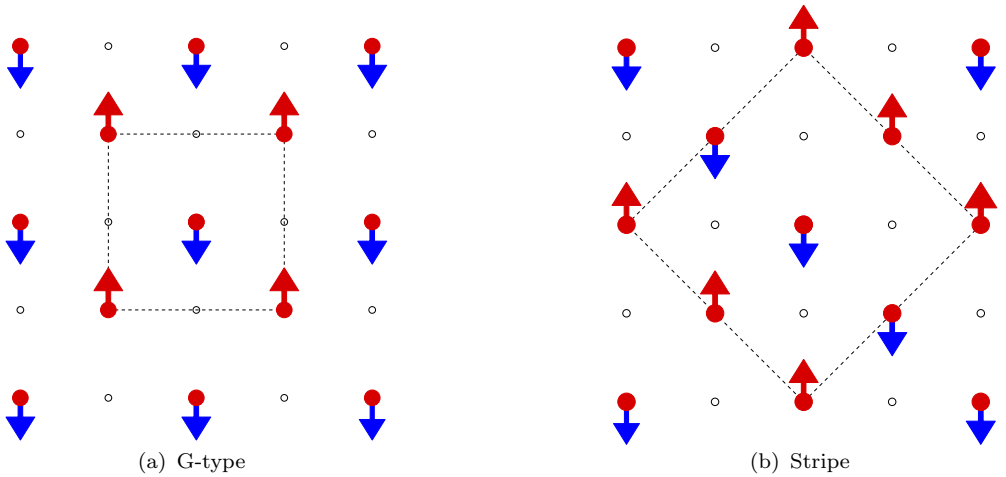

(a) G-type (b) Stripe

FIGURE 4.3: Schematic top views of two magnetic orders in the Mn-Mn layer and Fe-Fe layer respectively: (a) the conventional checkerboard antiferromagnetic *G-type* order (which is the ground state of $BaMn_2As_2$) and (b) the *stripe* antiferromagnetic order (ground state of $BaFe_2As_2$). The dashed squares denote the magnetic unit cells.

It was also found that the magnetic easy-axis direction in $BaMn_2As_2$ is along the *c*-axis, whereas it is in the *a*-*b* plane for $BaFe_2As_2$. Furthermore the magnetic transition is second order in $BaMn_2As_2$ in contrast to the first-order transition in $BaFe_2As_2$ [35, 36].

4.2.2 Magnetic moment

As already stated in the introduction, the experimental value of the ordered moment at $T = 10$ K is $\mu = 3.9\ \mu_B$/Mn. This value is considerably smaller than the value of 5.0 expected from $\mu = gS\mu_B$ for a fully localized picture. In the fully localized picture the atom resides in a single valence, therefore the ordered moment is equal to the atomic moment. Due to the strong Hund's rule interaction the spins of all five *d*-electrons are expected to be aligned, yielding a half-filled *d*-shell. In this high-spin state ($S = 5/2$) of

Mn^{2+} we are therefore expecting a net Mn moment of 5.0 μ_B/Mn (assuming a g factor $g = 2$), possibly reduced by quantum fluctuations. The reduction in $BaMn_2As_2$ mainly comes form the strong hybridization that results from the overlap between the Mn-d-orbitals and As-p-orbitals in this compound and can be seen in the density of states 4.7. In general, very strong hybridization is needed to effectively compete against the very strong Hund's interaction in the half-filled d shell of Mn^{2+}. So the hybridization between Mn-d and As-p states basically controls the Mn moment.
However the magnetic moment in $BaMn_2As_2$ is still much larger than the value of 0.9 μ_B/Fe found in $BaFe_2As_2$. In this compounds, the reduced moment on Fe is due to the itinerant nature of the magnetism. The large ordered moment on Mn indicate local moment antiferromagnetism in $BaMn_2As_2$, i.e. the ordered magnetic state displays a more localized behavior. This in turn suggests that electronic correlations in this system are stronger or at least more efficient in changing the electronic properties of the material.

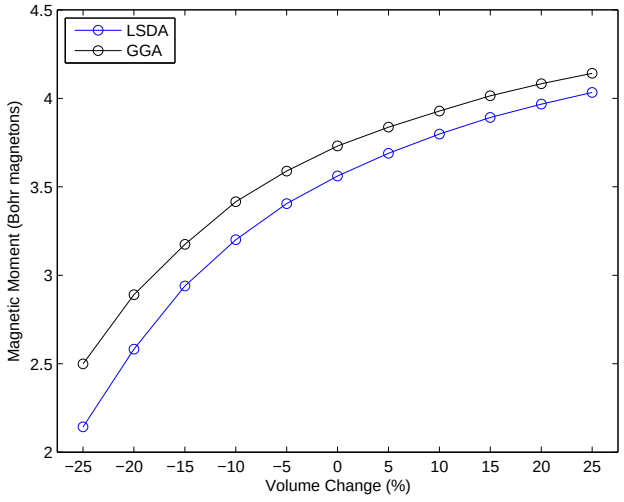

FIGURE 4.4: Dependency of the magnetic moment of the Mn-atoms on the unitcell volume. DFT calculations are done with two different exchange correlation potentials, LSDA and PBE-GGA.

DFT calculations of the ordered moment gives $\mu = 3.56\ \mu_B$/Mn for LSDA and 3.73 μ_B/Mn for GGA. The difference between the LSDA and GGA results is that the moment formation is a bit stronger in the GGA, but both values are still smaller than the experimental result. In fig. 4.4 the dependency of the magnetic moment on the lattice parameters is plotted. What can be seen is that the magnetic moment increases with increasing unit cell volume, i.e. with the Mn and As atoms being further apart. This reduction can be understood from hybridization of the Mn-d and As-p orbitals. With these two atoms being further apart, the hybridization decreases leading to an even more localized state

and a larger magnetic moment. On the other hand, a smaller unit cell volume that can be the result of an applied external pressure, leads to a smaller magnetic moment. So the Mn-As distance basically controls the overlap between the manganese and arsenide atoms and therefore controls the size of the magnetic moment by making the manganese electrons more localized (itinerant) with increasing (decreasing) distance.

4.2.3 Bandstructure and density of states

In the following section all density-functional calculations are done using LDA. A self-consistent density was generated with 726 k-points in the irreducible part of the Brillouin zone (all other k-points can be found using symmetry operations). The converged charge-density was then used to calculate energies along selected high-symmetry lines in the first Brillouin zone of the tetragonal lattice. The resulting band structures are shown in Fig. 4.5 for non-spin-polarized and antiferromagnetic ordered $BaMn_2As_2$, respectively. The corresponding densities of states are plotted in Figs. 4.6 and 4.7.

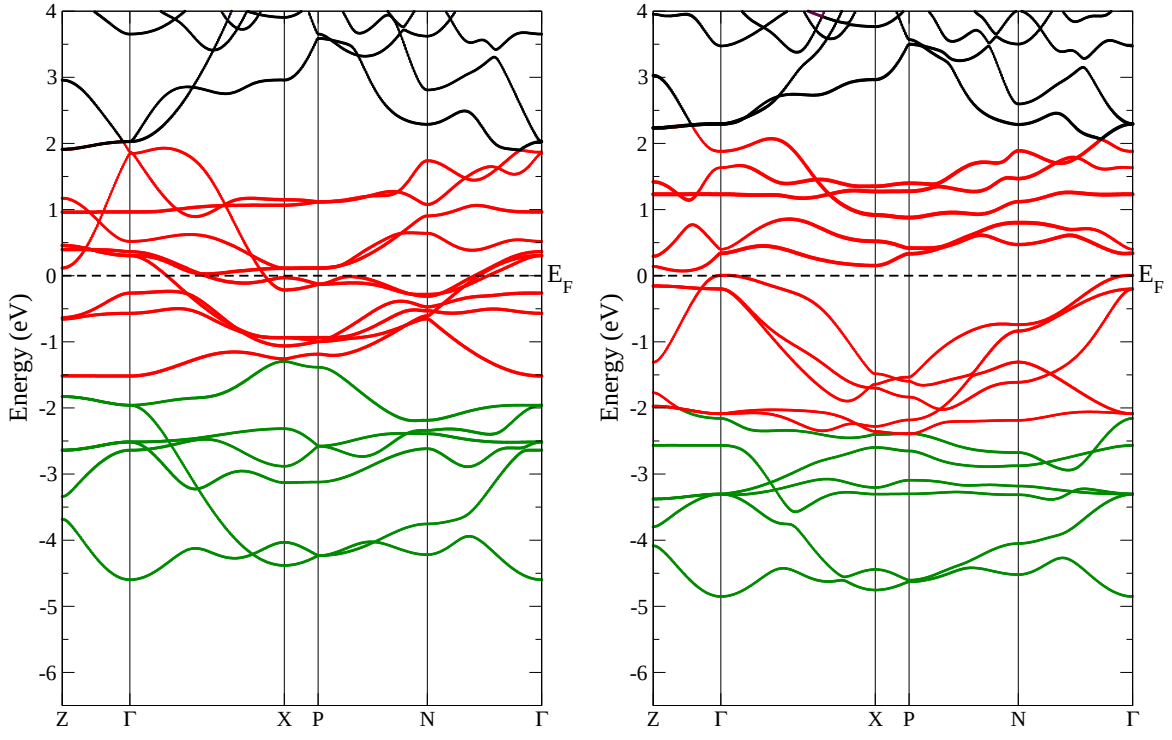

(a) non magnetic (b) antiferromagnetic

FIGURE 4.5: DFT-LDA bandstructure of $BaMn_2As_2$ in the paramagnetic (*left*) and antiferromagnetic phase (*right*) respectively. The manganese-3*d* states are highlighted in red and the arsenic-4*p* in green.

At first sight one can immediately see that the onset of magnetic order has a profound impact on the electronic structure. The non-spin-polarized band structure and DOS look very similar to that in $BaFe_2As_2$ only with a shifted Fermi energy due to the different electron count. For the understanding of the material properties it is important to identify the character of the dominant states near the Fermi level. LDA predicts that the dominant bands at the Fermi level come from Mn-3d states extending roughly between -1.5 eV and 2 eV, leading to a bandwidth of 3.5 eV as shown in Fig. 4.6. While the dominant electronic character near the Fermi level is due to Mn, a strong mixing with As states is apparent at -2.5 eV, where the As-4p band is peaked. The atom projected DOS confirms that there is a substantial hybridization between Mn-3d and As-4p states and there is virtually no contribution from Ba states in the region around the Fermi energy.
While the crystal field splitting in many transition metal oxides leads to a separation of transition metal d-bands into a t_{2g} and e_g part, this is not the case for $BaMn_2As_2$. All five Mn-d orbitals participate in the bonding, however, the orbitally resolved partial 3d DOS shows that at the Fermi energy the main contribution comes from the $t2g$-orbitals (xy and yz/zx) whereas the eg-orbitals ($3z^2$-r and x^2-y^2) have a minor weight.

The electronic structure with AFM order looks very different from the non-spin-polarized case. LDA already gives an insulation ground state with a small semiconducting gap of 0.1 eV. LDA calculations often underestimate band gaps, so it can be concluded that it is most likely the experimental band gap is somewhat larger than 0.1 eV. From AFM band-structure calculations one can also see the substantial hybridization between the Mn-3d and As-4p orbitals, which is responsible for the reduced ordered Mn moment. In fact from the AFM density of states it can be seen that the hybridization is spin dependent. The majority spin Mn-d states overlap in energy with the As-p states leading to a strong hybridization. The minority spin Mn-d states on the other side are above the main As-p DOS and are therefore less strongly mixed with the As states.

DFT-LDA gives us a metallic ground state in the non-spin-polarized case. However, experiments show that $BaMn_2As_2$ is a small gap semiconductor. In the next section we will investigate if correlation effects can lead to an insulating ground state even in the non-magnetic case. Therefore the non-spin-polarized calculation will be the staring point to perform LDA+DMFT calculations that will be treated in the next section.

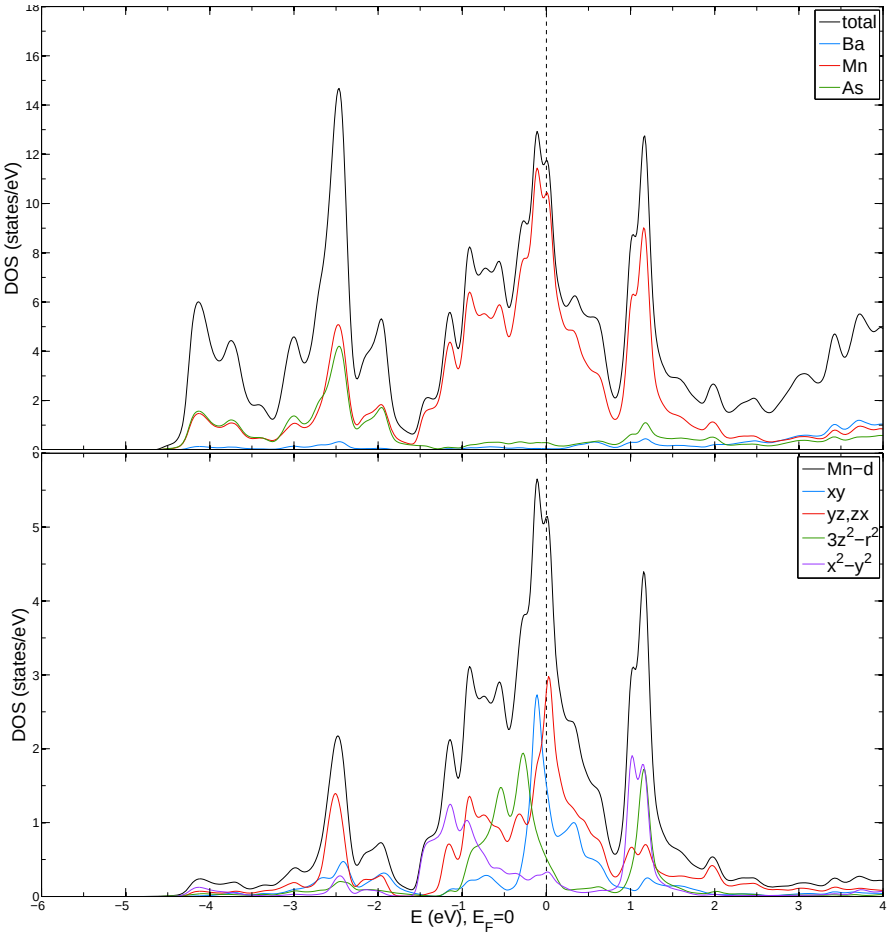

FIGURE 4.6: DFT-LDA density of states of $BaMn_2As_2$ in the paramagnetic phase. There is a hybridization between the manganese and arsenic orbitals.

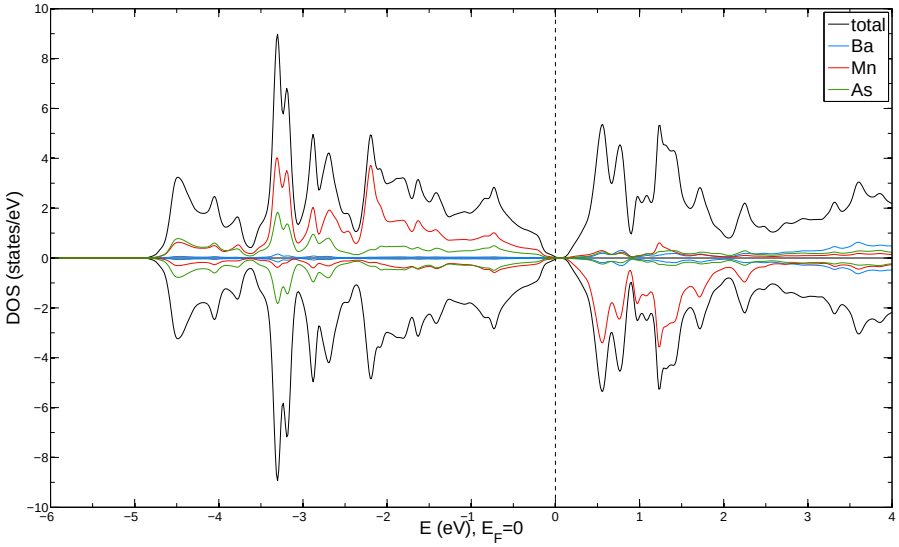

FIGURE 4.7: DFT-LSDA density of states of $BaMn_2As_2$ in the antiferromagnetic phase (*G-type*). DOS for majority spin is plotted above the axis and minority spin below.

4.3 Correlated electronic structure

For the calculation of the correlated electronic structure within the LDA+DMFT scheme, we use the WIEN2K+TRIQS code [28, 27]. In this code WIEN2K is used for the DFT calculation, the Kohn-Sham wave functions are then projected into the subspace of correlated orbitals for the DMFT calculation. The DMFT part is solved using the TRIQS package (*Toolbox for Research on Interacting Quantum Systems*) [41].

Technical aspects of our calculations

The impurity model within the DMFT loops was solved using a CT-QMC solver in the hybridization expansion version but only with density-density interactions to save computing time. All calculations are done at room temperature ($\beta = 40$ eV^{-1}, $T = 290$ K). There are several parameters that need to be set for the QMC process. The most important parameter is the number of Monte Carlo measurements N. In all calculations we used $N \sim 10^7$.

Once a fully charge self consistent LDA+DMFT calculation is running we need to define a criterion for the convergence of the QMC simulation. Since it is not easy to define an automated criterion we simply check the output self energy until we obtain a graphically converged solution over a few loops. The self energy curve has an increasing QMC error as the frequency increases, hence we fit the QMC data for Matsubara frequencies $i\omega > 80$. Fig. 4.8 is an example of a self energy obtained from a QMC simulation which is well-converged.

Once convergence of a calculation is achieved, it is desirable to quickly predict whether a metallic or insulating solution is obtained. The obvious way is to check directly the spectral function $A(\mathbf{k}, \omega)$ for spectral weight at the Fermi level. However to obtain the spectral function an analytical continuation of the QMC data onto the real frequency axis has to be performed, which again need non-negligible computation time especially if a large number of data points is considered. Therefore an indirect approach based on results in Matsubara frequency is desired.
One method is to check the imaginary part of the self energy as the Matsubara frequency approaches zero: $\Im[\Sigma(i\omega_n \rightarrow 0^0)]$. This gives an estimate value of the self energy at the real frequency zero. From the definition of the spectral function in terms of the self energy we can estimate the spectral weight at the Fermi energy as follows: For a metallic

solution we expect $\Im[\Sigma]$ to go to zero as ω approaches zero. On the other hand for an insulating solution the self energy should diverge for $\omega \to 0$. However, this is only valid in one-band systems. In multi-band systems it is a sufficient but not necessary condition for an insulating solution

A more direct method is to check the imaginary part of the Green function $G(i\omega_n \to 0^+)$ which corresponds to the retarded Green function at $\omega = 0$. $G(\omega)$ is directly connected to the spectral function at the Fermi energy through $A(\omega) = -\frac{1}{\pi}\Im[G(\omega)]$. For a metallic solution, $\Im[G(i\omega_n \to 0^+)]$ has some value corresponding to the spectral weight at the Fermi level, whereas for an insulation solution $\Im[G(i\omega_n \to 0^+)]$ goes to zero.

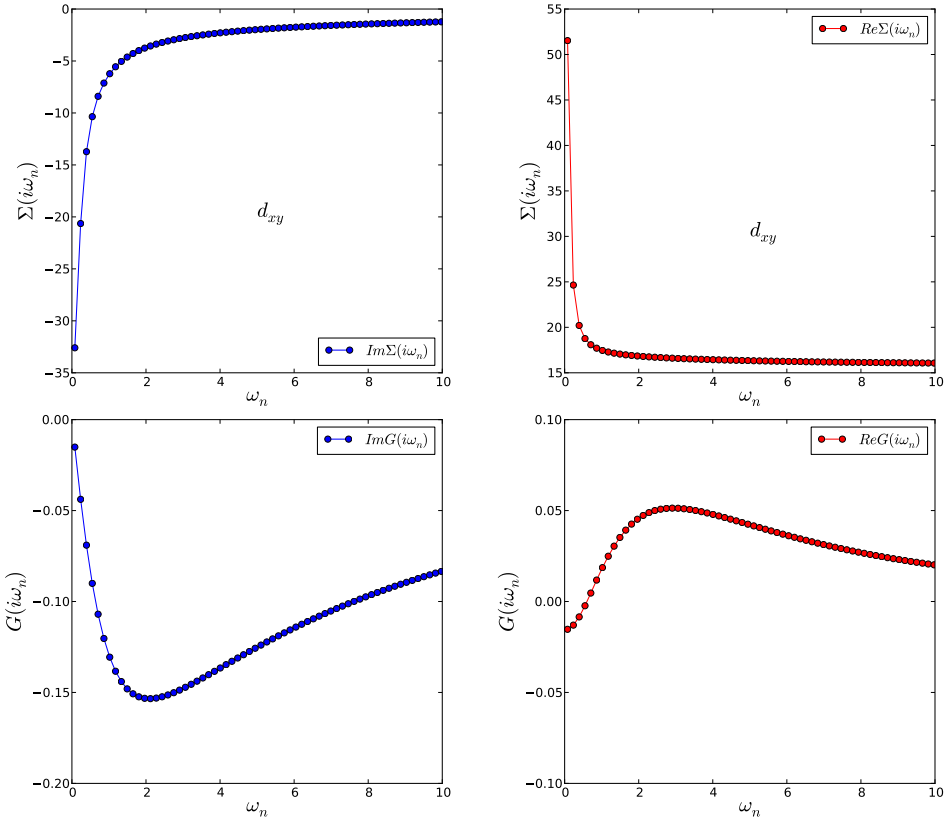

FIGURE 4.8: An example of the self energy (*top*) and the Green function (*bottom*) from a converged CT-QMC simulation that resulted in an insulating state. The imaginary parts are plotted on the *left* the real parts on the *right*. The calculation was done for $U = 4.0$ eV and $J = 0.9$ eV using FLL double counting correction with fixed $N = 5$ and an energy window of $\mathcal{W} = [-4.8; 2.2]$ eV.

Interaction parameters

The choice of the interaction parameters U and J is a crucial task within the LDA+DMFT method. In principle these values can be calculated from constrained local density approximation (cLDA) [42] or constrained random phase approximation (cRPA) [43] with a useful accuracy. However these values strongly depend on screening effects and therefore also on the included orbitals for the construction of the model Hamiltonian. This is why these parameters are often used as adjustable parameters to get the expected solution, in our case an insulation solution for the crystal structure of $BaMn_2As_2$. A major part of this work is to study the dependence of the result on the values of the interaction parameters U and J. As a starting point we use literature values form LDA+DMFT calculations of the isostructural iron pnictide $BaFe_2As_2$ [44, 45]. In the iron pnictides the electronic correlations are controlled by the Hund's exchange J, rather than by the Hubbard U. The Hund's rule interaction tends to align electrons when they find themselves on the same atom. We assume that also in the manganese based compound the Hund's exchange plays an important role in the context of correlations. Since the Mn-3d orbital should be exactly half-filled with 5 electrons, we believe the exchange energy to be higher than in the iron compound. Since it was shown that the manganese based compound is a more correlated material than its iron counterpart [46], we slightly increase the interaction parameters for our calculation in comparison to $BaFe_2As_2$-calculations. We estimate the effective on-site Coulomb parameter on the Mn-3d bands to be $U = 4.0$ eV and the intra-orbital exchange parameter to be $J = 0.9$ eV. Note that the bandwidth of the Mn-3d bands from LDA was around 4.5 eV, which is in the order of our estimate for Coulomb repulsion.

4.3.1 Choice of the energy window

In order to investigate the correlation effects in such complicated materials like $BaMn_2As_2$, it is important to have an optimized basis of localized Wannier functions. Therefore a suitable correlated subspace has to be chosen to perform a LDA+DMFT calculation. The correlated orbitals in the case of $BaMn_2As_2$ are the Mn-3d orbitals but because of the strong mixing with other states it is reasonable to use an extended energy window that also includes the ligand As-4p bands. The inclusion of the As-p bands is also physically motivated since charge-transfer effects might also play a role in the physics of the system. So an optimized basis of the localized dp Wannier functions is constructed from the 16

Bloch bands, corresponding to the 10 Mn-3d and 6 As-4p states. To capture all this states for this dp-model we need to choose an energy window that includes all these energy bands.
The right choice of the energy window is a crucial task within out formalism since it can strongly influence the result of the calculation. In fact one has to be very careful not to include bands that are not treated in the calculation. In the case of $BaMn_2As_2$ the LDA-bandstructure exhibits bands that lie above the ten Mn-d bands and originate form Ba states. Fatband plots indicated that these bands still show some Mn-d-character due to hybridization effects. However, LDA wrongly underestimates the gap between this Ba bands and the Mn bands and even predicts some mixing of these bands. We will show in the next section that for a correct description of the electronic structure within LDA+DMFT, the energy window has to be chosen such that it does not include bands above the correlated spectrum.

Influence of the energy window and the double counting

Next we discuss the consequences of wrongly including bands in the construction of our model lie above the Mn-d states. Furthermore the influence of the double counting correction will be investigated.
As stated above it is sometimes physically motivated to use an extended energy window. Due to mixing of correlated bands with other non-correlated bands it is sometimes not even possible to choose an energy window that does not include other bands but still capture the whole correlated spectrum. LDA often overestimates the hybridization of correlated and uncorrelated states resulting in a too strong mixing of the corresponding bands. For the dp-model we are therefore getting too many Mn-d electrons in our impurity problem if we are treating all occupied and unoccupied states. In fact from the energy-window $\mathcal{W} = [-4.8; 3.4]$ eV we get 6.2 electrons as initial occupancy for the impurity model, while the nominal value would be 5. Such a large deviation of the correlated electron count clearly do not properly reflect the correct physics of our material. A way out of this problem is to use an adequate double counting correction to shift the correlated bands relative to all other uncorrelated bands. The effect on the band structure is the following: In our implementation the chemical potential after each DMFT-loop is adjusted such that it yields the correct total number of electrons. Since the chemical potential has to lie within the Mn-d manifold, this means that the DC correction effectively shifts down all uncorrelated bands relative to the Fermi level. The amount of this shift

is directly given by the difference of the LDA and the LDA+DMFT chemical potential. This might reduce the number of electrons in the impurity problem closer to 5 electrons per Mn. However, note that the charge within realistic systems always be larger than five due to the covalency of chemical bonds.
In the top two graphics of Fig. 4.9 the **k**-resolved and the **k**-integrated spectral functions are plotted using AMF double counting and an extended energy window of $\mathcal{W} = [-4.8; 3.4]$ eV. One can see from the momentum integrated spectral function that there is almost a gap opening above the Fermi energy. Furthermore the As-p bands are shifted down by the determined LDA+DMFT chemical potential of $\mu = 1.06$ eV. Note that we measure the chemical potential relative to its LDA value. However this is not the expected result. We find a total charge inside the impurity problem to be 5.45 which is still more that the expected 5 electrons.
To overcome this problem we increase the DC shifting by setting the number of electrons to the fixed value of 5 electrons. This should further reduce the charge inside the impurity problem and give results close to experiment. The obtained spectral functions from this DC-shifting are plotted in the lower part of Fig. 4.9. It can be seen that we are still getting a bad metal instead of an insulator. The momentum resolved spectral function exhibits very clear bands around the Fermi level. However these bands have very little weight giving almost no states in a range of about 0.8 eV above the Fermi energy. As expected the As-p bands are further shifted down by the chemical potential of $\mu = 2.09$ eV and the charge inside the impurity problem is slightly reduced to 5.35. Now the question is where do the bands around the Fermi energy come from? The answer can be found by a comparison of the **k**-resolved spectral function with the LDA band structure. An accurate comparison shows that the bands around the Fermi energy look very similar to bands of the LDA band structure at around 2 eV. So the answer to the question is that not only the As-p bands are shifted further down by the chemical potential but also bands that were located above the Mn-d bands or are mixed with them are now getting shifted down creating states at the Fermi energy that should not exist. Note that a chemical potential of $\mu = 2.09$ eV means that bands are shifted down by this amount. These bands basically hinder the material from getting insulating. Further they are also wrongly influencing the chemical potential since μ is determined to reproduce the right total number of electrons in the system.

To summarize our findings the energy window should be chosen very carefully. In our case, Ba bands should not be included in the construction of a localized basis since they might drastically influence the solution by being shifted down to the Fermi level due to the

chemical potential resulting from the double counting correction. A correct description is therefore achieved by using the smaller energy window $\mathcal{W} = [-4.8; 2.0]$ eV. With this smaller energy window we can reduce the influence of empty higher bands, although these bands might show some Mn-d character in the LDA calculation.

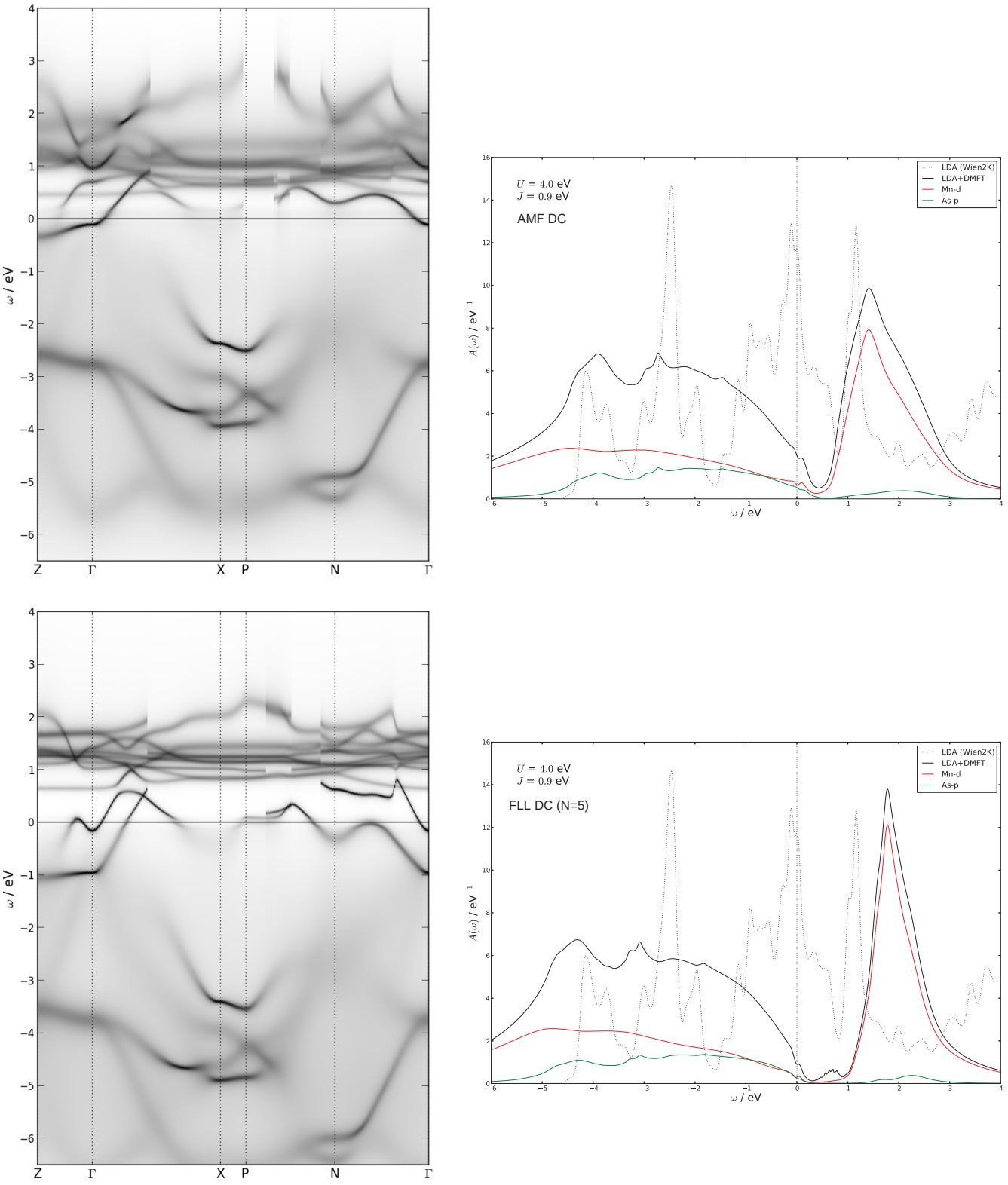

FIGURE 4.9: LDA+DMFT momentum resolved spectral function (*left*) and density of states (*right*) for $U = 4$ eV and $J = 0.9$ eV and an extended energy window of $\mathcal{W} = [-4.8; 3.4]$ eV. The results are plotted for conventional AMF double counting (*top*) and FLL double counting with fixed charge $N = 5$ (*bottom*).

4.3.2 Final results for non-magnetic $BaMn_2As_2$

We first focus on the non-spin-polarized case, not taking into account the magnetic ordering due to the significantly increasing complexity. For the calculations the FLL double counting correction with a fixed $N = 5$ is used, as it is believed to give better results for an insulating solution, which is what we expect from experiments. The results presented here are for interaction parameters $U = 4.0$ and $J = 0.9$. We used the dp-model with an energy window for the correlated subspace of $\mathcal{W} = [-4.8; 2.0]$. The obtained charge inside the impurity model is 5.15 and the determined chemical potential is $\mu = 2.16$ eV. Figures 4.10 and 4.11 show the momentum integrated and the momentum resolved spectral function respectively. Fig. 4.12 shows the orbitally resolved spectral functions for the five Mn-3d orbitals. The LDA density of states and band structure are also plotted for comparison. One can immediately see that our result gives an insulating state with a band gap of about 0.7 eV. The As-4p bands can still be recognize from LDA band structure, however, due to the double counting correction they are shifted down by the chemical potential of $\mu = 2.1$ eV. The Mn-3d bands are divided into a lower and a upper Hubbard band. The upper Hubbard bands shows a clearly peaked structure above the Fermi energy. In the momentum resolves spectral function individual bands can still be recognized. In contrast the bands of the lower Hubbard band are completely smeared out and mixed with the As-p states. Therefore no clear lower Hubbard band can be seen.

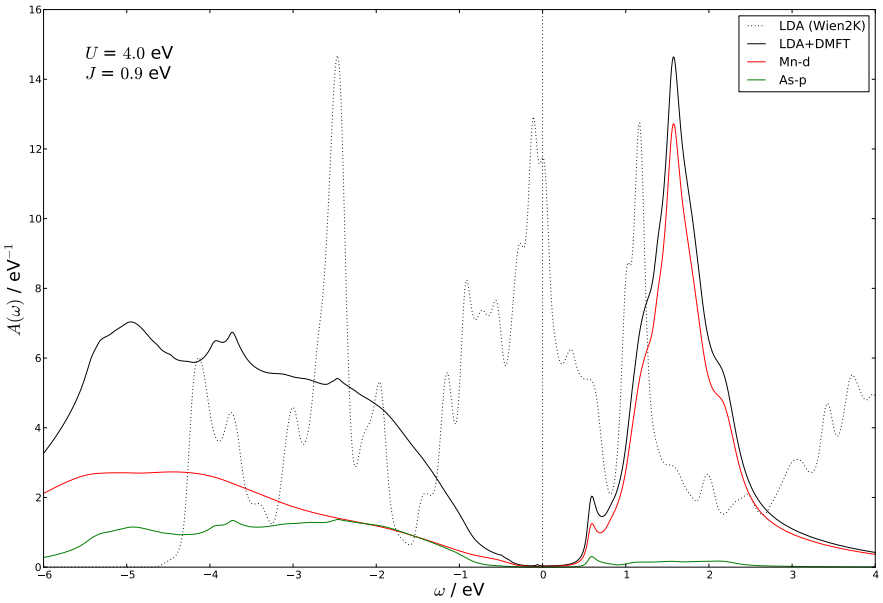

FIGURE 4.10: LDA+DMFT density of states of non-magnetic $BaMn_2As_2$ compared with LDA. Further the correlated DOS is orbitally resolved for Mn-3d and As-4p states.

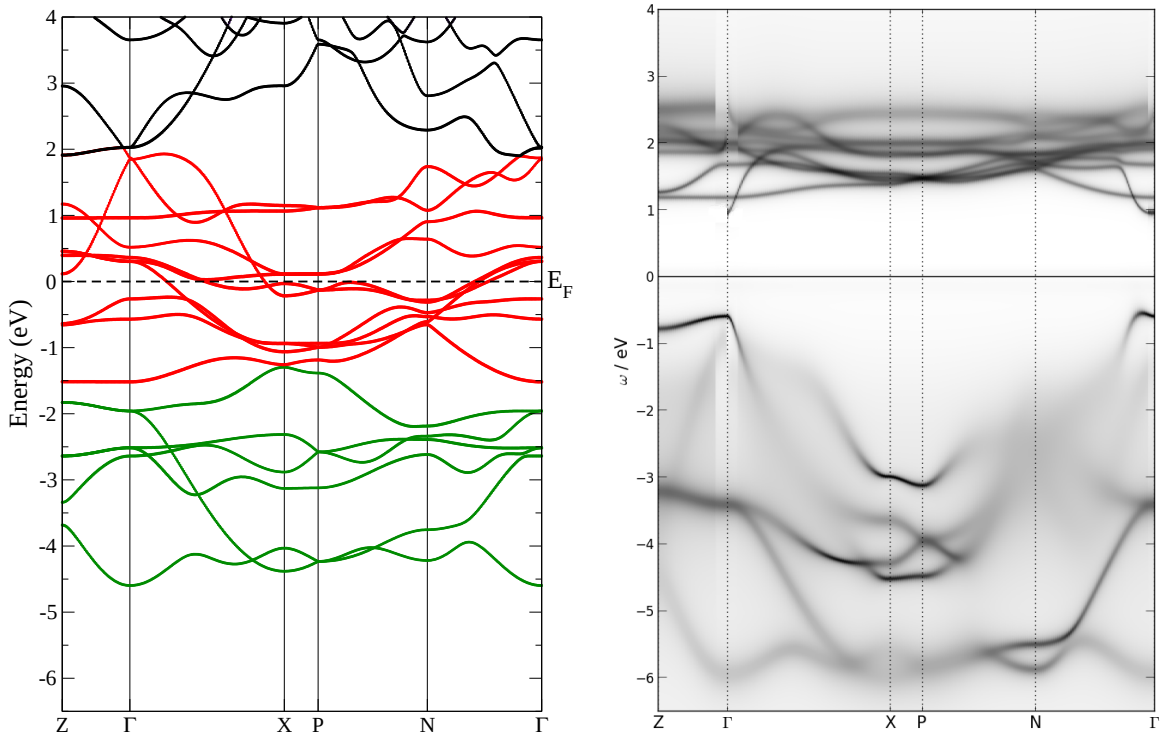

(a) LDA (b) LDA+DMFT

FIGURE 4.11: Comparison of LDA bandstructure (*left*) and DMFT momentum resolved spectral function (*right*) of non-magnetic $BaMn_2As_2$.

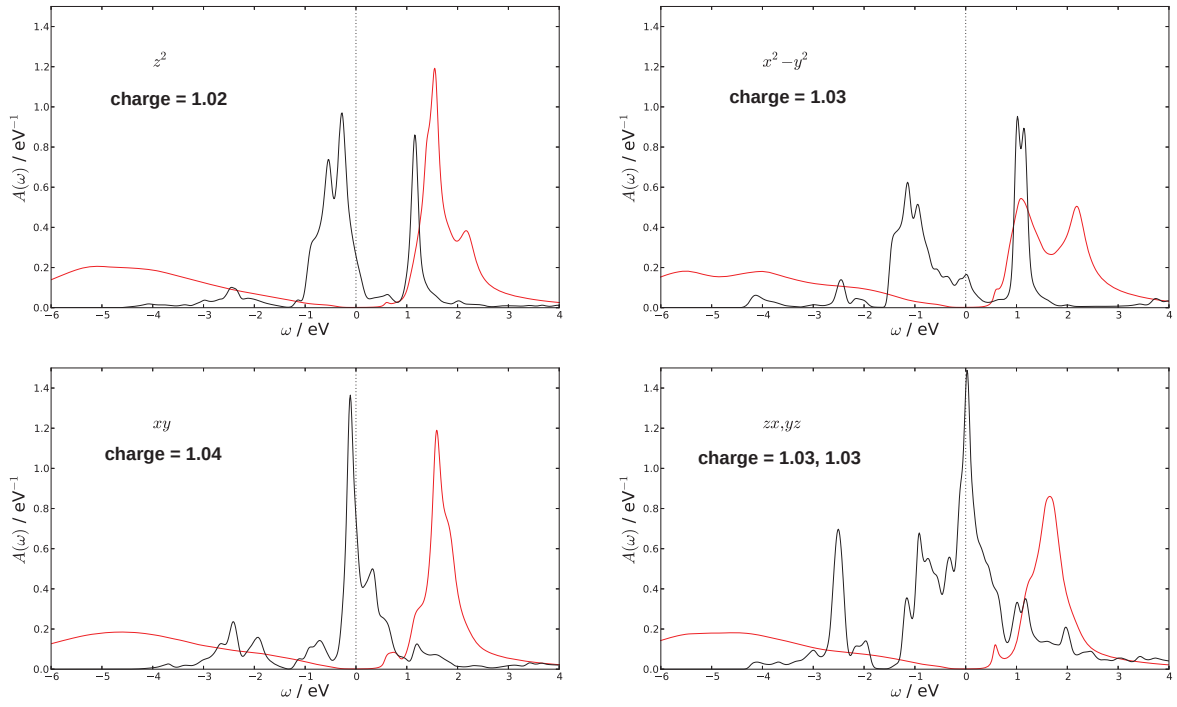

FIGURE 4.12: Orbitally resolved Mn-3*d* density of states of non-magnetic $BaMn_2As_2$ (*red*) compared with LDA (*black*).

From the orbitally resolved spectral functions of the five Mn-d orbitals in Fig. 4.12 one can see that the local orbital occupations are almost equal for all five orbitals and close to one electron per orbital. This is due to the fact that the Hund's rule coupling tends to equalize the local orbital occupations. In our case all five d orbitals become close to half-filled as the system goes through the Mott transition. This fact strongly indicates the importance of the Hund's exchange coupling in manganese pnictides.

We also investigated the influence of Hubbard U and Hund's exchange J on the size o the band gap. Therefore we first fixed the exchange parameter to $J = 0.9$ eV and performed calculations for various U. It turned out that already a smaller Hubbard interaction of $U = 3.0$ eV leads to an insulating state in the paramagnetic phase of $BaMn_2As_2$. In fact for constant J we observed a linear increase of the band gap with increasing U. In the range of $U = 3.0 - 5.0$ eV the band gap grows linearly from 0.4 eV up to 1.0 eV. We can conclude that the insulating state quite robust and not sensitive to small variation of Hubbard U.
On the other hand we found that the system is more sensitive to changes of the exchange coupling J. It is easy to change the ground state from insulating to metallic by modifying J. We can say that our results show a stronger dependence of the physical properties of the system on the Hund's exchange J rather than Hubbard U.

4.3.3 Magnetic calculations

Until now we only investigated the paramagnetic phase in $BaMn_2As_2$. However we know from experiments that this compound is in an antiferromagnetically ordered state up to a temperature of 625 K. In general the properties of transition-metal compounds are known to be controlled by a strong and complex interplay between electronic and magnetic degrees of freedom. Therefore for an adequate description of the electronic structure in $BaMn_2As_2$ it would be crucial to also consider magnetism and not only electronic correlations.
Starting point for magnetic LDA+DMFT calculations is a converged non-spinpolarized LDA calculation. In the non-magnetic calculations before we always forced the solution into a non-magnetic state by symmetrizing the spin-up and spin-down solutions before each new DMFT circle. This is necessary to prevent the calculation from running into a magnetic solution that cannot be stabilized. For an antiferromagnetic calculation we cannot consider just one Mn atom in the unit cell and transfer the result to the second

Mn-atom by symmetry operations anymore. Now the Mn sites in the unit cell needs to be treated as inequivalent sites which further increases the complexity of the problem. Starting from a converged non-magnetic LDA calculation the development of the spin-dependent charge distribution inside the impurity model as a function of the DMFT iteration step is plotted in Fig. 4.13. It seems that the system favors an antiferromagnetic state, however, it was not possible to stabilize our calculations to achieve a converged solution. The moment is somehow oscillating around, sometimes being constant over a few loops. It seems that there is one meta-stable charge configuration in which the system tends to stay longer than in other configurations (e.g. in cycle five). This solutions corresponds to a magnetic moment of $\mu = 2.2\ \mu_B$/Mn, which would be in the range of values measured from neutron diffraction experiments at around 530 K [35]. This is of course a quite crude estimation from which we clearly cannot really conclude that our LDA+DMFT calculation yields the right magnetic moment. However, we can conclude that the material tends to prefer an antiferromagnetic solution, although we are unfortunately not able to present converged results for this phase.

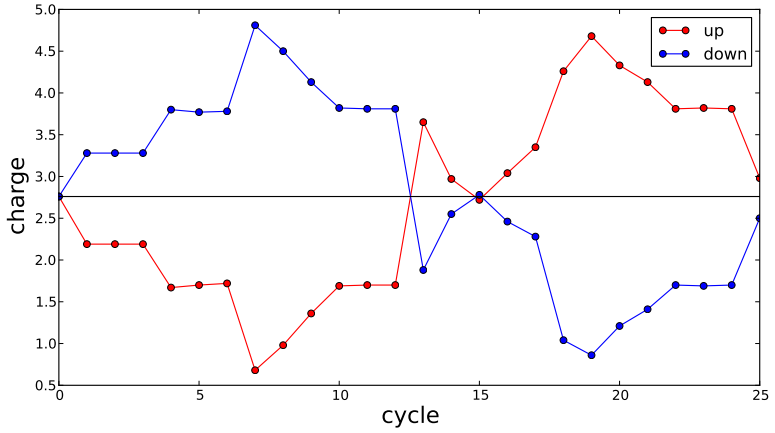

FIGURE 4.13: Total Charge inside the impurity model for spin up (*red*) and spin down (*blue*) electrons plotted over a few DMFT loops.

4.4 Conclusion and Outlook

In conclusion, we studied the electronic structure of the manganese bases pnictide material $BaMn_2As_2$. We calculated the orbital and momentum resolved spectral function of the compound with the LDA+DMFT method for interaction parameters $U = 4.0$ eV and $J = 0.9$ eV. LDA predicts that in the paramagnetic case the Mn-3d bands are crossing the Fermi level with no clear splitting into the eg and $t2g$ manifold. We showed that local electronic correlations among the five electrons in the set of five Mn-3d orbitals are strong enough to push the compound into an insulating phase with a band gap of 0.7 eV. We conclude that LDA+DMFT basically is an adequate method to describe the electronic structure of this strongly correlated material in the paramagnetic phase.
However, for a complete description of the electronic structure in $BaMn_2As_2$ the magnetic order must be considered as well. Experiment show that below 625 K $BaMn_2As_2$ in an antiferromagnetic ordered state. Spin-polarized LDA correctly predicts an AFM semiconducting ground state, however, the LDA band gap is to small in comparison to experiments and electronic correlations are known to play an important role in transition metal compounds. Reaching a converged solution for the magnetic states was not achieved in our work, although in principle it should be possible within the LDA+DMFT framework.
A correct description of the magnetic and electronic structure of $BaMn_2As_2$ might also require some non-local correlations which can be treated within a cluster LDA+DMFT approach, but we leave this question open for future work.

Chapter 5

LaMnAsO

5.1 Introduction and crystal structure

The second Mn-based pnictide compound we study in this thesis is LaOMnAs. It is iso-structural to the parent compound of the iron pnictide superconductor LaOFeAs and belongs to the oxypnictides or so-called 1111 family of these compounds. It was a breakthrough for these materials when superconductivity at 26 K was found in $La[O_{1-x}F_x]FeAs$ in 2008 [30]. However, no superconductivity was found in LaOMnAs so far, although it was believed to be a promising candidate for high temperature superconductivity since its physical properties show strong similarities to those of the parent compounds of cuprate high T_C superconductors. As in the case of $BaFe_2As_2$ the suppression of the antiferromagnetic phase transition that goes along with a orthorombic distortion seems to be important for superconductivity. But unlike LaOFeAs the antiferromagnetic phase seems to be very robust in LaOMnAs and no orthorombic distortion is observed.

LaMnAsO crystallizes in a quasi two-dimensional tetragonal ZrCuSiAs structure (space group *P4/nmm*), consisting of alternating layers of LaO and MnAs [47, 48]. Every manganese is surrounded by four arsenic atoms and DFT calculations show that there is a substantial hybridization between the the Mn-3*d* and As-4*p* orbitals. The Lanthanum and oxygen atoms are situated far enough in space from the Mn ions and therefore their electronic states are weakly hybridizing with the Mn-*d* states.
LaOMnAs is a localized moment AFM insulator with a Néel temperature of about 317 K, and a magnetic moment of 3.34 μ_B/Mn (at 2 K) that is ordered parallel to the *c* axis [48]. The saturated moment is comparable to that for $BaMn_2As_2$ and it is reduced

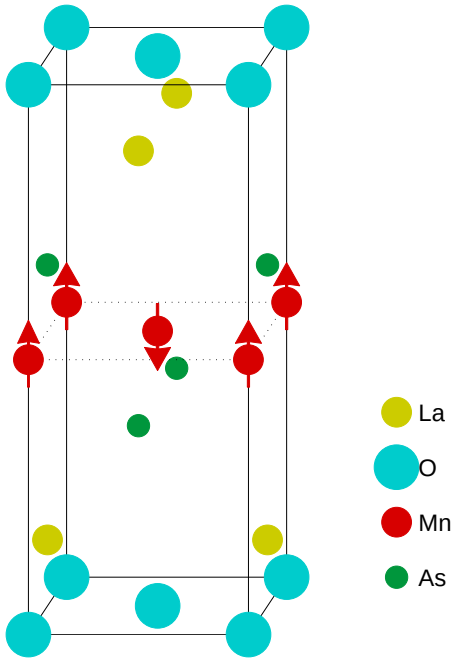

FIGURE 5.1: Crystal and magnetic structure of LaOMnAs with *P4/nmm* space group symmetry. The arrows indicate the direction of the magnetic moments of the Mn atoms in the antiferromagnetically ordered state.

from the theoretical value of 5.0 μ_B/Mn as a result of the substantial hybridization between the Mn-3*d* and the As-4*p* orbitals. In contrast, LaOFeAs is an AFM semi-metal with T_N = 137 K and an ordered magnetic moment of 0.36 μ_B/Fe [30, 49]. Similar to $BaMn_2As_2$, LaOMnAs can be metalized by chemical substitution, e.g hole doping on the La site [50], still keeping AFM order. It is generally believed that the Hund's rule coupling in Mn compounds is so strong that doping will not reduce the correlations to the point at which the antiferromagnetic phase transition is suppressed and superconductivity may become possible [51].

5.2 *ab initio* DFT calculations

Again WIEN2K was used to calculate first *ab initio* properties of the studied material LaOMnAs. Literature values were used for the lattice parameters [47]: a = 4.1188 Å and c = 9.0441 Å with internal parameters $z_{As} = 0.6684$ and $z_{La} = 0.1326$. Calculations were performed within the LDA using 630 k-points in the irreducible Brillouin zone (with 8 symmetry operations this leads to 10,000 k-points in the full Brillouin zone).

A total energy calculation confirmed the ground state of LaOMnAs being a AFM *G-type* similar to $BaMn_2As_2$.

Bandstructure and density of states

The band structures along selected high-symmetry lines in the first Brillouin zone are plotted in Fig. 5.2 for non-spin-polarized and AFM ordered LaOMnAs, respectively. Figs. 5.3 and 5.4 show the corresponding density of states. Again there is a significant difference in the electronic structure of the two different phases.

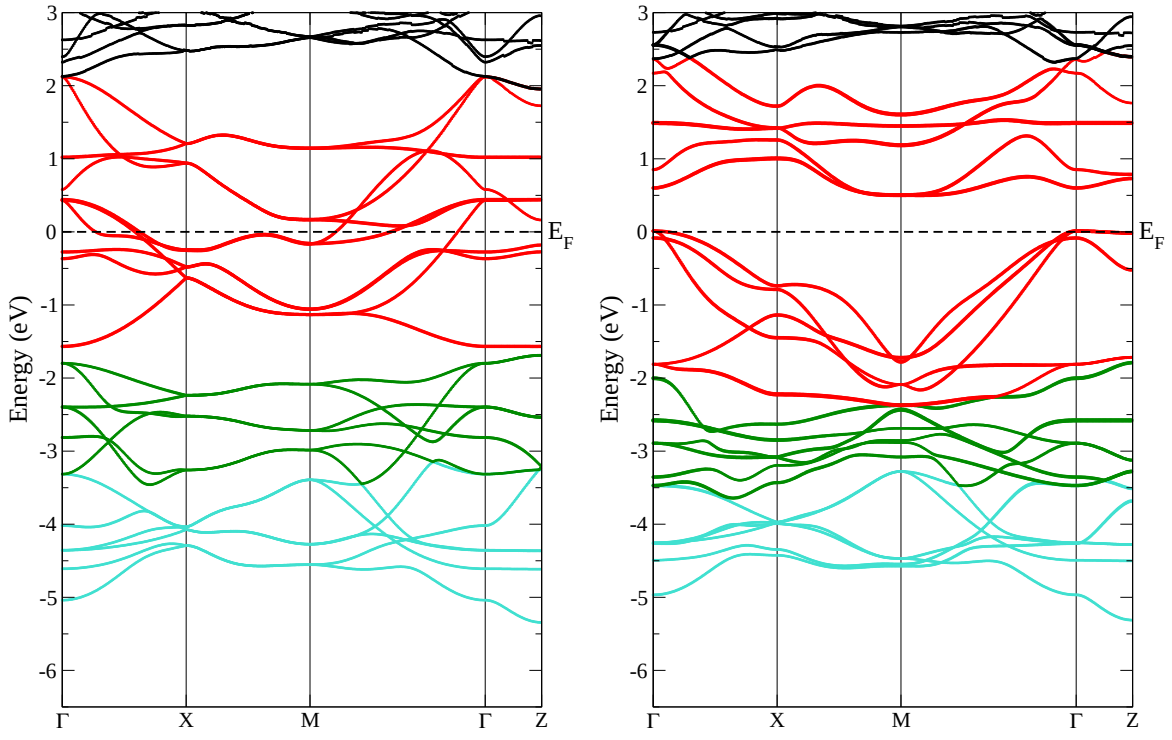

(a) non magnetic (b) antiferromagnetic

FIGURE 5.2: DFT-LDA Bandstructure of LaOMnAs in the paramagnetic (*left*) and antiferromagnetic phase(*right*), respectively. The manganese-3*d* bands are highlighted in red, the arsenic-4*p* in green and the oxygen-2*p* bands in blue.

From the non-spin-polarized calculation we are getting a metal with predominantly Mn-*d* states at the Fermi level, particularly t_{2g}-orbitals (xy and yz/zx) rather than the e_g-orbitals ($3z^2$-r and x^2-y^2). In the region between -1.7 and -2.8 eV mixing between the Mn-3*d*, As-4*p* and O-2*p* states can be found, leading to a hybridization between these orbitals. However, Mn-*d* fatband plots indicate that in the non-magnetic case the

hybridization is weaker than in $BaMn_2As_2$. There is even a small band gap between the As-4p and Mn-3d bands. Below -2.8 eV the main contribution to the DOS comes from the oxygen. In this region the O states also mix with the La states, but there is virtually no hybridization between La and Mn.

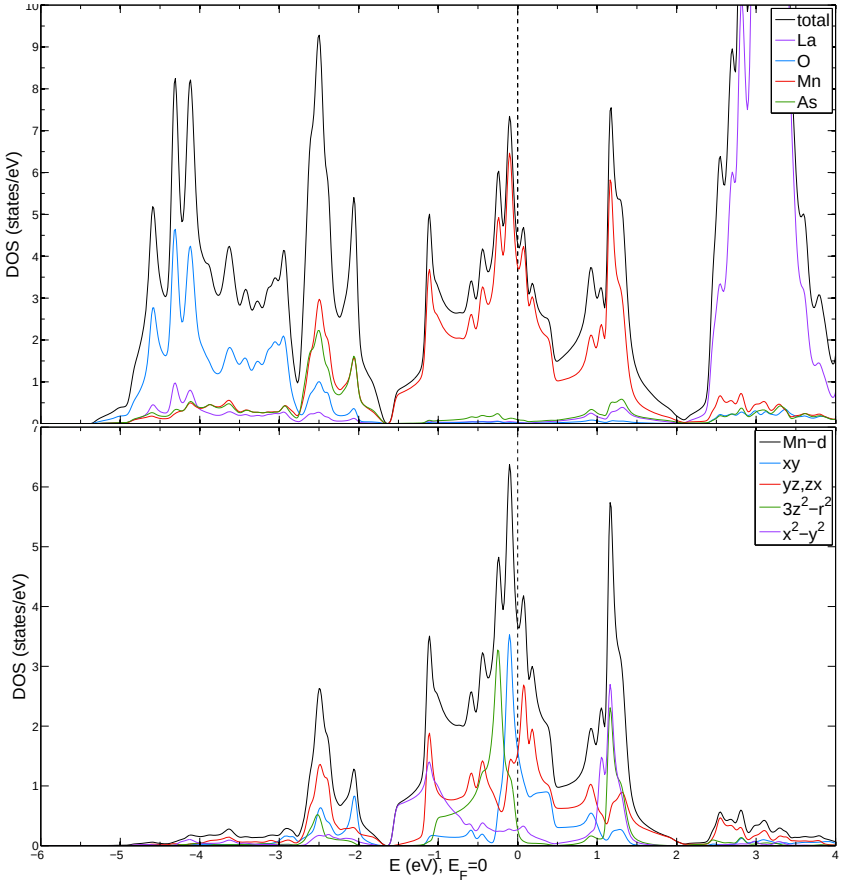

FIGURE 5.3: DFT-LDA density of states of LaOMnAs in the paramagnetic phase.

Whereas a non-spin-polarized calculations wrongly gives a metal, the AFM calculation results in an insulating state with a bandgap of approximately 0.4 eV. This corresponds to the experimentally found ground state indicating that magnetism plays an important role in this material. However, the LDA value of the bandgap is much smaller than the value obtained from experiment. Optical measurements suggested that LaOMnAs is a indirect-transition-type semiconductor with an indirect band gap of approximately 1.4 eV [52]. LDA typically underestimates the bandgap within a few percent, but this huge deviation from the experimental value indicates, that electronic correlations have to be considered to correctly describe the electronic structure in LaOMnAs.

The value of the magnetic moment obtained from LDA is 3.66 μ_B/Mn and therefore slightly too large in comparison to the experiment value of 3.34 μ_B/Mn at low temperatures. This is in contrast to the LDA calculations for $BaMn_2As_2$ that resulted in a too

small magnetic moment. In the AFM case we again find a spin-dependent hybridization for the Mn-*d* states. The majority spin states overlap with the As-*p* and O-*p* states, whereas the main contribution of the minority spin states lies above the Fermi energy and therefore does not hybridize with other states.

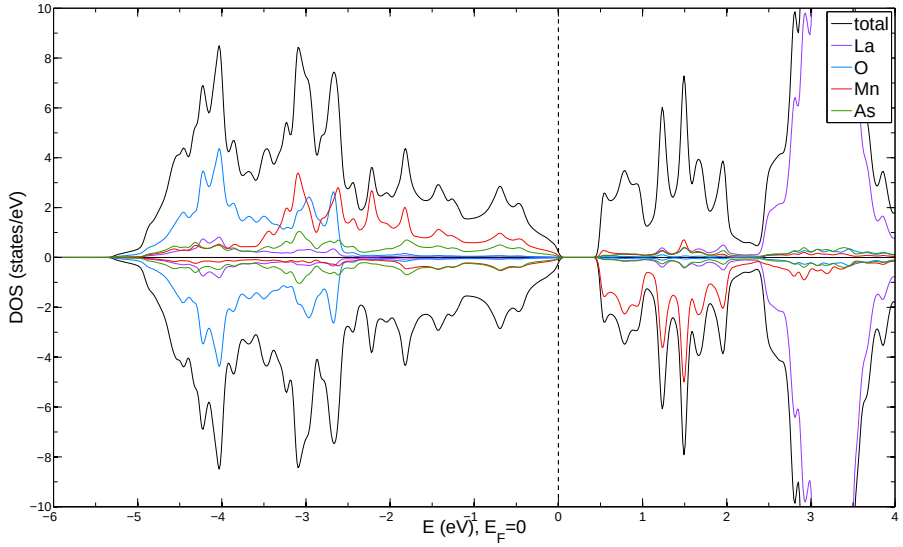

FIGURE 5.4: DFT-LSDA density of states of LaOMnAs in the antiferromagnetic phase (*G-type*). DOS for majority spin is plotted above the axis and minority spin below.

5.3 Correlated electronic structure

In this section we are using the fully charge self-consistent implementation of LDA+DMFT combining WIEN2K with the TRIQS package. The impurity model is solved with a CT-QMC solver in the hybridization expansion at the inverse temperature $\beta = 40\ \mathrm{eV}^{-1}$ (room temperature $T = 290$ K).
We are only investigating the correlated electronic structure in the paramagnetic phase of LaOMnAs. The correlated model Hamiltonian for the DMFT loop is constructed from the non-spin-polarized LDA result. In contrast to $BaMn_2As_2$ the Mn-d bands of LaOMnAs are separated from the lower lying As and O bands by a small band gap. Also the higher lying La bands only show minor mixing with the Mn bands. This makes it easier to choose an energy window including only the correlated Mn-3d bands and construct a localized basis only from these d bands. This d-model, however, in not capable to capture hybridization nor charge transfer effects. From the LDA density of states one can see that there is in fact a hybridization of Mn with As orbitals as well as with O orbitals. Therefore it would be physically motivated to use a *dpp*-model constructed from Mn-3d, As-4p and O-2p bands. In the following sections we will present the difference of these two models on describing the correlated electronic structure in LaOMnAs.

5.3.1 The *dpp*-model

In the *dpp*-model hybridization effects of the correlated d-states with other orbitals are taken into account by the choice of the energy window. For the construction of the localized basis we use a total of 22 bands, including 10 Mn-3d, 6 As-4p and 6 O-2p bands. The chosen energy window for this *dpp*-model is $\mathcal{W} = [-5.5; 2.2]$ eV. The selected bands are highlighted in the LDA bandstructure in Fig. 5.2.
To be able to compare LaOMnAs with $BaMn_2As_2$ we use the same interaction parameter as for the *dp*-model in $BaMn_2As_2$: $U = 4.0$ eV and $J = 0.9$ eV (although a different screening is expected). We used the normal FLL double-counting correction (without fixing the number of electrons to $N = 5$), which is meant to be more appropriate for insulating systems. In Fig. 5.5 we plotted the resulting spectral function together with the corresponding LDA density of states. From the DOS near the Fermi level we can see that the material is still metallic. But is seem we are close to a Mott metal-insulator transition as a band gap is almost opening up. This behavior is similar to our results for $BaMn_2As_2$ without DC-shifting. With the choice of the energy window we are not

having the problem of bands being shifted down to the Fermi level due to the chemical potential. Therefore there must be an other reason for not getting an insulating state. A reason might be the underestimation of the p-d gap between As and Mn bands. This explanation is supported by the fact that the final charge inside the impurity problem is 5.5 which is quite far away from the nominal number of electrons in the Mn-d orbital of five. As in the case of $BaMn_2As_2$ we could use a double-counting shifting to manually increase the p-d gap. However, one needs to be careful in using such manually adjusted DC correction for increasing the p-d gap since its justification is still controversial.
Fig. 5.6 shows the correlated momentum resolved spectral function $A(\mathbf{k}, \omega)$ on the right together with the LDA band structure on the left. One can see that the As-p states hybridize strongly with the Mn-d states and get, thus, affected by correlations. The O-p bands on the other hand remain almost unchanged since they hybridize much less with Mn-d. Therefore we can well identify the oxygen bands that are shifted down due to the obtained chemical potential of $\mu = 1.02$ eV in comparison to the LDA band structure. The lower part of the As-p spectrum is also not much influenced by correlations. As we are reaching the As bands that are mixed with the correlated Mn states the bands are getting more diffuse until no well-defined bands can be identified. The spectrum above the Fermi energy is governed by quite flat and therefore localized Mn bands.

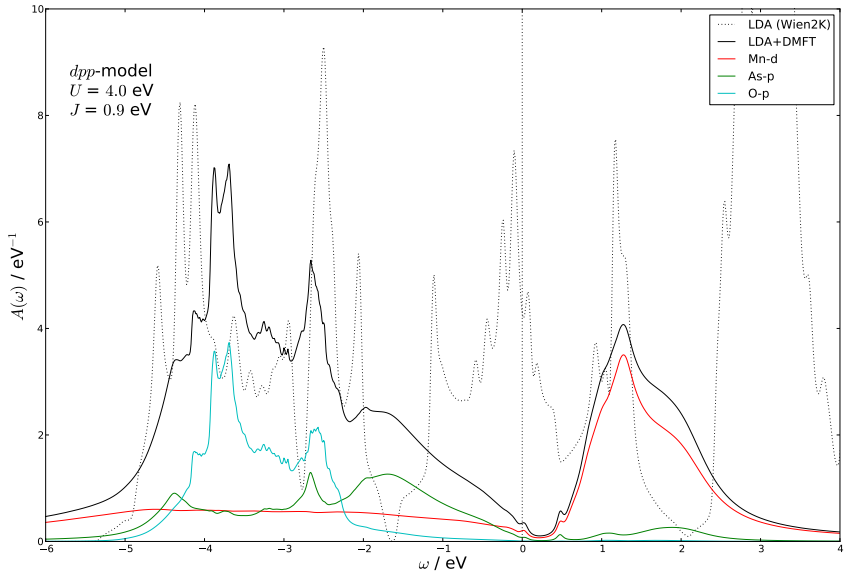

FIGURE 5.5: LDA+DMFT density of states of non-magnetic LaOMnAs compared with LDA-DOS. Further the correlated DOS is orbitally resolved for Mn-3d, As-4p and O-2p states.

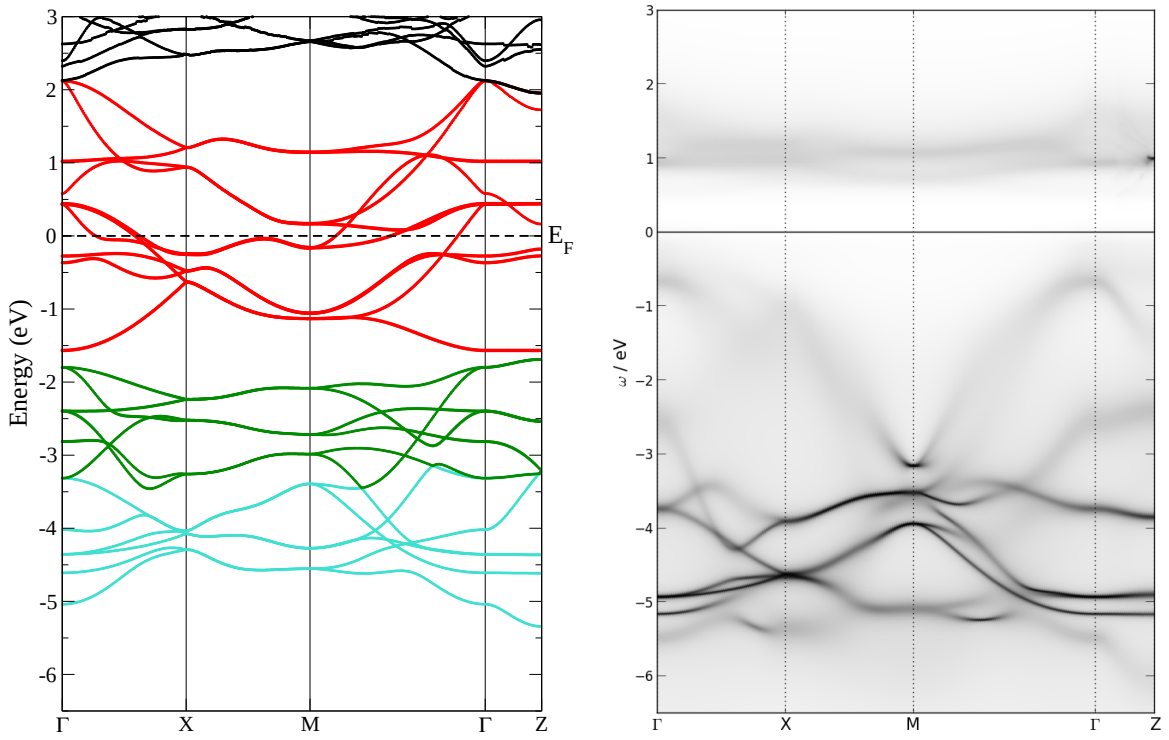

FIGURE 5.6: Comparison of LDA bandstructure (*left*) and DMFT momentum resolved spectral function (*right*) of non-magnetic LaOMnAs.

5.3.2 The *d*-model

For the *d*-model we only use the 10 Mn-3*d* bands within the energy window $\mathcal{W} = [-1.6; 2.2]$ eV. We automatically get the initial charge of 5.0 inside the energy window which corresponds to five Mn electrons in the five Mn-3*d* orbitals. The values of the initial charge distribution from LDA of the five orbitals are: 1.30, 1.15, 0.85, 0.85 for d_{z^2}, $d_{x^2-y^2}$, d_{xy} and degenerate $d_{zx,yz}$ orbitals, respectively. This means that the charge is not equally distributed over the *d* orbitals.

Without the screening from other non-correlated hybridized orbitals we expect the correlations to be stronger than for a full *dpp*-model. To reproduce the experimental band gap of 1.4 eV [52] we will investigate the dependence of the electronic structure on the correlation strength. For this model the double counting should not have any influence on the results since for a *d*-only model the DC can be absorbed in the chemical potential. For the calculations we used a DC correction of the FLL type.

To investigate how the electronic structure depends on the correlation strength, we fixed the J/U ratio to 0.225 and performed calculations from ($J = 0.3$, $U = 1.3$) eV up to

($J = 0.9$, $U = 4.0$) eV. A selection of resulting Mn-d resolved spectral functions are plotted in Fig. 5.7. As comparison the Mn-d partial LDA density of state is plotted in the graphs as well. One can see that in the region of weak correlations we basically reproduce the LDA result. As expected it is much easier to open a band gap if we are only considering the Mn-d bands rather than in the full *dpp*-model. Already for the rather small interaction parameters ($J = 0.5$, $U = 2.2$) eV LaOMnAs is in a Mott insulating phase. One can clearly see the lower and upper Hubbard bands, separated by a band gap of about 0.8 eV, which is typical for Mott insulators. As we are going through the Mott transition the charge distribution in all five Mn-d orbitals is getting equalized due to the Hund's rule coupling leading to half filled electron orbitals. As we increase the interaction strength the Hubbard bands basically keep the same shape but the band gap increases up to 3.8 eV.

We can summarize that a LDA+DMFT calculation taking into account only the d orbitals is capable of reproducing the insulating behavior of LaOMnAs. With the right choice of the interaction parameters we were able to correctly reproduces the experimental size of the band gap. However, dealing with the Mn-d spectrum only introduces quite severe approximations. The physics of charge transfer and hybridization effects cannot be captured without taking into account the ligand p states. Further due to the small energy window the Wannier functions are getting quite extended leading to non-local Coulomb interactions. Therefore it is questionable if a calculation treating only the correlated d orbitals gives a reasonable description of the studied material.

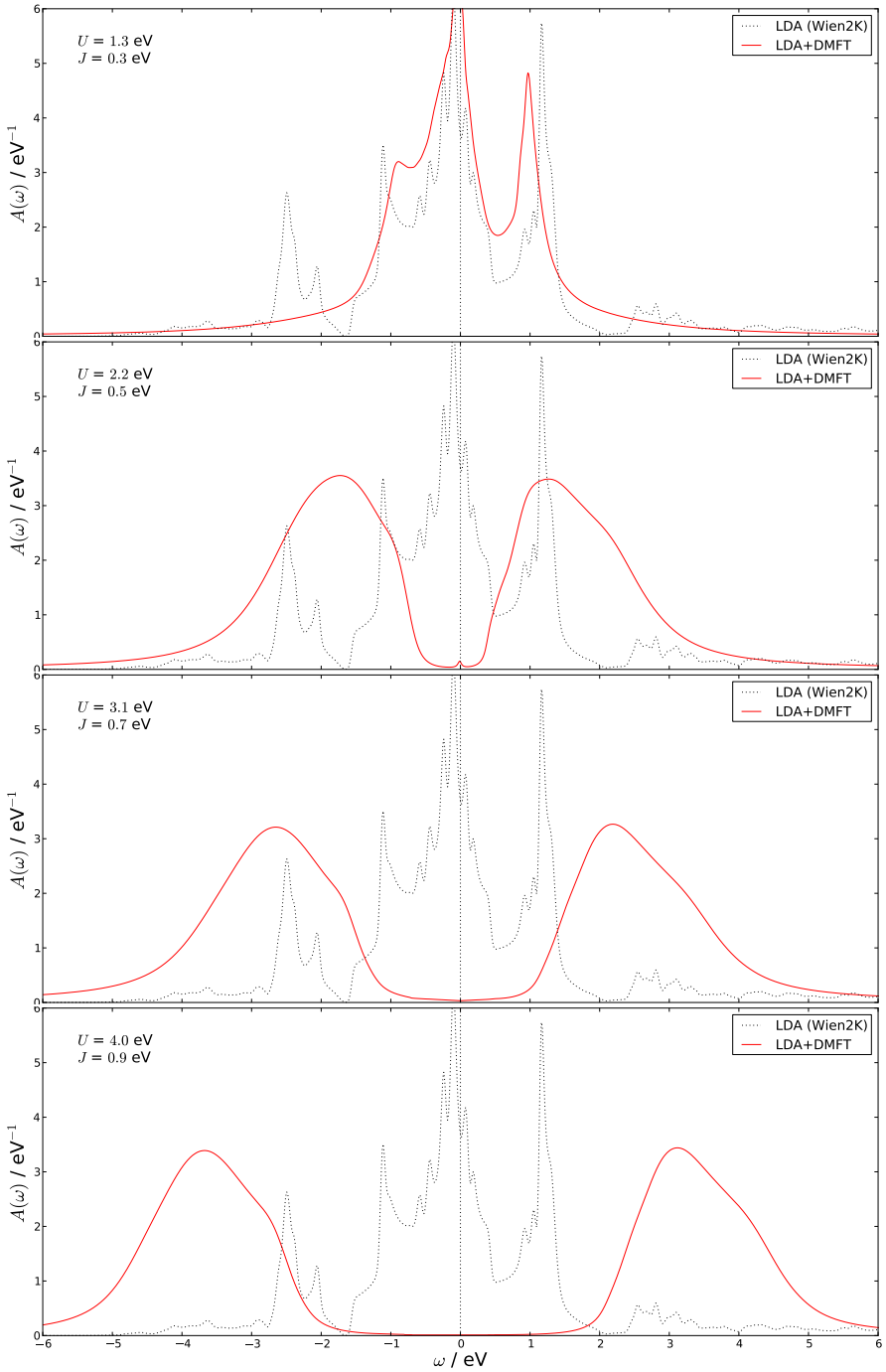

FIGURE 5.7: DMFT density of states of non-magnetic LaOMnAs for different correlations strengths in the d-model compared with partial Mn-d LDA-DOS.

5.4 Conclusion and Outlook

LDA calculations do not properly describe the electronic structure of LaOMnAs since it fails to capture effects that originates from strong electronic correlations. LDA gives a metallic state in the paramagnetic phase but already correctly predicts an insulating antiferromagetically ordered ground state. However, the LDA band gap is to small in comparison to experiments and electronic correlations are known to play an important role in transition metal compounds. Therefore we applied the LDA+DMFT method to calculate the correlated electronic structure of paramagnetic LaOMnAs for interaction parameters $U = 4.0$ eV and $J = 0.9$ eV. Our LDA+DMFT results for the *dpp*-model indicate that in this correlation regime LaOMnAs is close to an insulating Mott state.
We also performed calculations with a smaller energy window that includes Mn-d bands only. In this model we were able to show the Mott metal-insulator transition taking place already for relatively small interaction parameters of $U = 2.2$ eV and $J = 0.5$ eV. However, the smaller energy window results in more extended Wannier functions that might lead non-local Coulomb interactions. Therefore the physical validity of this simplified model is questionable.
Finally we were not able to stabilize calculations in the experimentally observe antiferromagetically ordered state to investigate the interplay of electronic and magnetic degrees of freedom in LaOMnAs.

Bibliography

[1] Hohenberg, P. & Kohn, W. Inhomogeneous electron gas. *Phys. Rev.* **B136**, 864–871 (1964).

[2] Kohn, W. & Sham, L. Self-consistent equations including exchange and correlation effects. *Phys. Rev.* **A140**, 1133–1138 (1965).

[3] Ceperley, D. & Alder, B. Ground state of the electron gas by a stochastic method. *Phys. Rev. Lett.* **45**, 566–569 (1980).

[4] Perdew, J. *et al.* Atoms, molecules, solids, and surfaces: Applications of the generalized gradient approximation for exchange and correlation. *Phys. Rev. B* **46**, 6671–6687 (1992).

[5] Perdew, J., Burke, K. & Ernzerhof, M. Generalized gradient approximation made simple. *Phys. Rev. Lett.* **77**, 3865–3868 (1996).

[6] Schwarz, K., Blaha, P. & Madsen, G. Electronic structure calculations of solids using the WIEN2K package for material sciences. *Computer Physics Communications* **147**, 71–76 (2002).

[7] Schwarz, K. & Blaha, P. Solid state calculations using WIEN2K. *Computational Materials Science* **28**, 259 – 273 (2003).

[8] Cottenier, S. *Density Functional Theory and the family of (L)APW-methods* (2013).

[9] Andersen, O. Linear methods in band theory. *Phys. Rev. B* **12**, 3060–3083 (1975).

[10] Singh, D. *Planewaves, Pseudopotentials, and the LAPW Method* (Kluwer Boston, 1994).

[11] Mott, N. *Metal Insulator Transitions* (Taylor & Francis, 1990), 2nd edn.

[12] Imada, M., Fujimori, A. & Tokura, Y. Metal-insulator transitions. *Rev. Mod. Phys.* **70**, 1039–1263 (1998).

[13] Anisimov, V., Zaanen, J. & Andersen, O. Band theory and mott insulators: Hubbard U instead of stoner *I*. *Phys. Rev. B* **44**, 943–954 (1991).

[14] Anisimov, V., Aryasetiawan, F. & Lichtenstein, A. First-principles calculations of the electronic structure and spectra of strongly correlated systems: the LDA+U method. *Journal of Physics: Condensed Matter* **9**, 767 (1997).

[15] Anderson, P. W. Localized magnetic states in metals. *Phys. Rev.* **124**, 41–53 (1961).

[16] Metzner, W. & Vollhardt, D. Correlated lattice fermions in $d = \infty$ dimensions. *Phys. Rev. Lett.* **62**, 324–327 (1989).

[17] Georges, A. & Kotliar, G. Hubbard model in infinite dimensions. *Phys. Rev. B* **45**, 6479–6483 (1992).

[18] Georges, A., Kotliar, G., Krauth, W. & Rozenberg, M. Dynamical mean-field theory of strongly correlated fermion systems and the limit of infinite dimensions. *Rev. Mod. Phys.* **68**, 13–125 (1996).

[19] Gull, E. *et al.* Continuous-time monte carlo methods for quantum impurity models. *Rev. Mod. Phys.* **83**, 349–404 (2011).

[20] Werner, P., Comanac, A., de Medici, L., Troyer, M. & Millis, A. Continuous-time solver for quantum impurity models. *Phys. Rev. Lett.* **97**, 076405 (2006).

[21] Werner, P. & Millis, A. Hybridization expansion impurity solver: General formulation and application to kondo lattice and two-orbital models. *Phys. Rev. B* **74**, 155107 (2006).

[22] Jarrell, M. & Gubernatis, J. Bayesian inference and the analytic continuation of imaginary-time quantum monte carlo data. *Physics Reports* **269**, 133–195 (1996).

[23] Lichtenstein, A. & Katsnelson, M. Ab initio calculations of quasiparticle band structure in correlated systems: LDA+U approach. *Phys. Rev. B* **57**, 6884–6895 (1998).

[24] Georges, A. Strongly correlated electron materials: Dynamical mean-field theory and electronic structure. In *American Institute of Physics Conference Series*, vol. 715 of *American Institute of Physics Conference Series*, 3–74 (2004).

[25] Anisimov, V. & Y.Izyumov. Electronic structure calculations for real materials by LDA+DMFT method. In *Electronic Structure of Strongly Correlated Materials*, vol. 163 of *Springer Series in Solid-State Sciences*, 203–251 (Springer Berlin Heidelberg, 2010).

[26] Anisimov, V. *et al.* Full orbital calculation scheme for materials with strongly correlated electrons. *Phys. Rev. B* **71**, 125119 (2005).

[27] Aichhorn, M. *et al.* Dynamical mean-field theory within an augmented plane-wave framework: Assessing electronic correlations in the iron pnictide lafeaso. *Phys. Rev. B* **80**, 85101 (2009).

[28] Aichhorn, M., Pourovskii, L. & Georges, A. Importance of electronic correlations for structural and magnetic properties of the iron pnictide superconductor lafeaso. *Phys. Rev. B* **84**, 54529 (2011).

[29] Czyzyk, M. & Sawatzky, G. Local-density functional and on-site correlations: The electronic structure of la_2cuo_4 and $lacuo_3$. *Phys. Rev. B* **49**, 14211–14228 (1994).

[30] Kamihara, Y., Watanabe, T., Hirano, M. & Hosono, H. Iron-based layered superconductor $LaO_{1-x}F_xFeAs$ with $T_c = 26$ K. *J. of Am. Chem. Soc.* **130**, 3296–3297 (2008).

[31] Rotter, M., Tegel, M. & Johrendt, D. Superconductivity at 38 k in the iron arsenide $Ba_{1-x}K_xFe_2As_2$. *Phys. Rev. Lett.* **101**, 107006 (2008).

[32] Johnston, D. The puzzle of high temperature superconductivity in layered iron pnictides and chalcogenides. *Advances in Physics* **59**, 803–1061 (2010).

[33] Mani, A., Ghosh, N., Paulraj, S., Bharathi, A. & Sundar, C. Pressure-induced superconductivity in $BaFe_2As_2$ single crystal. *EPL (Europhysics Letters)* **87**, 17004 (2009).

[34] Pandey, A. *et al.* Coexistence of half-metallic itinerant ferromagnetism with local-moment antiferromagnetism in $Ba_{0.60}K_{0.40}Mn_2As_2$. *Phys. Rev. Lett.* **111**, 047001 (2013).

[35] Singh, Y. *et al.* Magnetic order in $BaMn_2As_2$ from neutron diffraction measurements. *Phys. Rev. B* **80**, 100403 (2009).

[36] Huang, Q. *et al.* Neutron-diffraction measurements of magnetic order and a structural transition in the parent $BaFe_2As_2$ compound of FeAs-based high-temperature superconductors. *Phys. Rev. Lett.* **101**, 257003 (2008).

[37] Kitagawa, K., Katayama, N., Ohgushi, K., Yoshida, M. & Takigawa, M. Commensurate itinerant antiferromagnetism in $BaFe_2As_2$. *J. of Phys. Soc. of Jap.* **77**, 114709 (2008).

[38] Satya, A. *et al.* Pressure-induced metallization of $BaMn_2As_2$. *Phys. Rev. B* **84**, 180515 (2011).

[39] Pandey, A. *et al.* $Ba_{1-x}K_xMn_2As_2$: An antiferromagnetic local-moment metal. *Phys. Rev. Lett.* **108**, 087005 (2012).

[40] Birch, F. Finite elastic strain of cubic crystals. *Phys. Rev.* **71**, 809–824 (1947).

[41] Ferrero, M. & Parcollet, O. TRIQS: a Toolbox for Research in Interacting Quantum Systems. URL `http://ipht.cea.fr/triqs`.

[42] Anisimov, V. I. & Gunnarsson, O. Density-functional calculation of effective coulomb interactions in metals. *Phys. Rev. B* **43**, 7570–7574 (1991).

[43] Aryasetiawan, F. *et al.* Frequency-dependent local interactions and low-energy effective models from electronic structure calculations. *Phys. Rev. B* **70**, 195104 (2004).

[44] Yin, Z., Haule, K. & Kotliar, G. Magnetism and charge dynamics in iron pnictides. *Nature Phys.* **7**, 294 (2011).

[45] Skornyakov, S., Anisimov, V. & Vollhardt, D. Microscopic origin of the linear temperature increase of the magnetic susceptibility of $BaFe_2As_2$. *Phys. Rev. B* **86**, 125124 (2012).

[46] Yao, Y., Schmalian, J., Wang, C., Ho, K. & Kotliar, G. Comparative study of the electronic and magnetic properties of $BaFe_2As_2$ and $BaMn_2As_2$ using the gutzwiller approximation. *Phys. Rev. B* **84**, 245112 (2011).

[47] Emery, N. *et al.* Giant magnetoresistance in oxypnictides LaOMnAs. *Chem. Commun.* **46**, 6777–6779 (2010).

[48] Emery, N. *et al.* Variable temperature study of the crystal and magnetic structures of the giant magnetoresistant materials LMnAsO(L = La, Nd). *Phys. Rev. B* **83**, 144429 (2011).

[49] Nomura, T. *et al.* Crystallographic phase transition and high-t_c superconductivity in LaFeAsOF. *Superconductor Science and Technology* **21**, 125028 (2008).

[50] Sun, Y. *et al.* Insulator-to-metal transition and large thermoelectric effect in $La_{1-x}Sr_xMnAsO$. *EPL (Europhysics Letters)* **98**, 17009 (2012).

[51] Suzuki, H. *et al.* Absence of superconductivity in the hole-doped fe pnictide $ba(fe_{1-x}mn_x)_2as_2$: Photoemission and x-ray absorption spectroscopy studies. *Phys. Rev. B* **88**, 100501 (2013).

[52] Kayanuma, K., Hiramatsu, H., Kamiya, T., Hirano, M. & Hosono, H. Epitaxial film growth and optoelectrical properties of layered semiconductors, LaMnXO (X=P, As, and Sb). *J. of Appl. Phys.* **105**, 073903 (2009).

Abbreviations

AFM	**A**ntif**e**rro**m**agnetic
AMF	**A**round **M**ean **F**ield
cLDA	**c**onstrained **L**ocal **D**ensity **A**pproximation
cRPA	**c**onstrained **R**andom **P**hase **A**pproximation
CT-QMC	**C**ontinuous **T**ime - **Q**uantum **M**onte **C**arlo
DC	**D**ouble **C**ounting
DFT	**D**ensity **F**unctional **T**heory
DMFT	**D**ynamical **M**ean **F**ield **T**heory
FLL	**F**ully **L**ocalized **L**imit
GGA	**G**eneralized **G**radient **A**pproximation
(L)APW+lo	(**L**inearized) **A**ugmented **P**lane-**W**ave + **l**ocal **o**rbitals
L(S)DA	**L**ocal (**S**pin) **D**ensity **A**pproximation
SIAM	**S**ingle **I**mpurity **A**nderson **M**odel

Acknowledgements

I would like to express my gratitude to my supervisor, Prof. Dr. Enrico Arrigoni, for giving me the opportunity to work on this very interesting and emerging topic.
I specially thank Dr. Markus Aichhorn for his guidance and for answering all of my questions. I benefited very much from his experience and knowledge. Without his supervision and constant help this thesis would not have been possible.
I would also like to thank all members of the *Institute of Theoretical and Computational Physics* for their support and providing a good atmosphere at the office.
Finally, thanks to my family and my friends at the university and beyond, who have supported me throughout the entire process. Specially, I would like to thank my parents for their unconditional support, both financially and emotionally throughout my entire studies.